American Mineralogist, Volume 110, pages 154-170, 2025

Miyake-jima anorthite: A lunar crustal material analog

Arkadeep Roy[1,*], Ananya Mallik[1], Kerri Donaldson Hanna[2], Tyler J. Goepfert[3], and Richard L. Hervig[3]

[1]Department of Geosciences, University of Arizona, 1040 E 4th Street, Tucson, Arizona 85721, U.S.A.
[2]Department of Physics, University of Central Florida, 4111 Libra Drive, Orlando, Florida 32816, U.S.A.
[3]School of Earth & Space Exploration, Arizona State University, 550 E Tyler Mall, Tempe, Arizona 85287-1404, U.S.A.

Abstract

High-calcic (~95% anorthite) plagioclase is the key mineral comprising the primary lunar crustal suites that cover over 60% of the Moon's surface. Pristine crystals of similar high-calcic plagioclase are rare occurrences on Earth, which creates a roadblock to using terrestrial material as lunar crustal analogs. We discuss the potential of a particular megacrystic anorthite ($An_{95.51\pm0.31}$) occurring in the basaltic lava flows of the island arc volcano in Miyake-jima, Japan, as a material analog. A comprehensive analytical routine for the Miyake-jima anorthites has been performed to explore intra- and inter-crystalline heterogeneities in major, minor, and trace elements. These anorthites show flat concentration gradients across core profiles for all major elements (Si, Al, Ca, Na), minor elements (Mg, Fe), and most trace elements (La, Ce, Pm, Nd, Eu). Comparing the chemical composition of the samples with that of different lunar crustal suites like ferroan anorthosites, high-magnesium suites, and high-alkali suites shows that the Miyake-jima anorthites are overlapping or depleted in most minor and trace elements except for a slight enrichment in Li, Ti, Fe, Sr, Eu, Ba, and Pb. Given the low abundance of most trace elements in the Miyake-jima anorthites, we can treat this sample suite as a "blank slate," which provides the opportunity to dope the crystalline matrix with the elements of interest at different levels and use them for geochemical, petrologic, and spectroscopic studies. The lack of typical magmatic zoning and overlapping elemental compositions across the different megacrysts make the Miyake-jima anorthites very well suited as a lunar crustal material analog. Highly calcic, crystalline anorthite is shown to have unique spectral signatures from less calcic anorthite, and intermediate and sodic compositions of plagioclase feldspar as calcium and iron contents control the wavelength position and shape of the diagnostic spectral features in the thermal infrared region of the electromagnetic spectrum. Thus, near- and thermal infrared spectral measurements of the Miyake-jima anorthites highlight the importance of developing chemically and mineralogically consistent terrestrial material analogs for remote sensing studies.

Keywords: Natural anorthite megacrysts, lunar material analog, major and trace elements, near-infrared and thermal infrared spectra

Introduction

Plagioclase feldspar, specifically anorthite (An), is the most dominant mineral in the ferroan anorthosites (FAN), which constitute the lunar highlands (Dowty et al. 1974). The highlands comprise almost all the lunar farside and large sections of the lunar nearside crust. The plagioclase in FAN is compositionally restricted to $An_{94–98}$ and contains minor Fe-rich pyroxenes, which led to their FAN nomenclature (Dowty et al. 1974; McGee 1993). Traces of olivine, silica, chromite, ilmenite, and spinel in the FAN suites have also been reported. The widespread distribution of highly anorthitic plagioclase on the Moon's surface is due to the preservation of large sections of the primary lunar crust, which is thought to have crystallized from the late magma ocean (Smith et al. 1970; Wood et al. 1970; Walker and Hays 1977; Warren 1985; Shearer 2006; Grove and Krawczynski 2009). In contrast, Earth's primary crust has been expunged through recycling and secondary crust-building processes (Herzberg and Rudnick 2012; Foley et al. 2002). Although typical terrestrial anorthosite massifs have >90% modal abundance of plagioclase, these monomineralic rocks are not associated with high-calcic plagioclase. The increase in modal plagioclase is generally associated with mineral compositions becoming more labradoritic (Bowen 1917). Smaller ophitic anorthite crystals ($An_{90–100}$) are commonly encountered in island arcs (Arculus and Wills 1980; Brophy 1986), intraoceanic forearcs (Falloon and Crawford 1991), and mid-ocean ridge basalts (Donaldson and Brown 1977; Stakes et al. 1984) typically forming under water-saturated conditions (Sisson and Grove 1993). Therefore, a dearth of naturally occurring large and pristine ~An_{95} plagioclase crystals exists, which limits their use as a potential lunar material analog for geochemical, spectroscopic, geophysical, and experimental petrology studies. There have been previous attempts at developing Stillwater anorthosite as a potential lunar material analog (Salpas et al. 1983). However, the anorthite content (or An#, which is the molar Ca/[Ca + Na + K] ratio of plagioclase) of most plagioclase from the Stillwater complex varies from $An_{69–83}$, which is less calcic than lunar FAN, rendering them a poorly suited material analog. In addition, the Stillwater anorthosites show

* Corresponding author E-mail: arkadeeproy@arizona.edu

0003-004X/25/0001–154$05.00/DOI: https://doi.org/10.2138/am-2023-9122-a

zoning and overgrowth that amplify the intracrystalline heterogeneity, making it difficult to focus on the study of pristine lunar anorthosites.

Trace element partitioning in plagioclase is dependent on the anorthite content, which exerts control on the lattice strain parameters (Drake and Weill 1975; Blundy and Wood 1991; Bindeman et al. 1998, 2007; Bindeman and Davis 2000; Bédard 2006; Tepley et al. 2010; Dohmen and Blundy 2014; Sun et al. 2017). The strong crystal-chemical dependence in the plagioclase mineralogy requires any potential lunar crustal material analog involving the study of trace elements to have the closest match in terms of anorthite content. In addition, this warrants the justification for detailed characterization of trace element geochemistry of a potential lunar material analog for both experimental petrology and spectroscopic studies.

The rare occurrence of megacrysts of anorthite ($An_{97}Ab_3$) was first reported within the basaltic lava flows of Mt. Hyoutanyama on the island arc volcano of Miyake-jima in the Izu islands of Japan (Kikuchi 1888). The anorthites have ~0.5% FeO and are often noted to be coated by red-wine-colored hematite crystallites (Isshiki 1958; Smith and Brown 1988; Arakawa et al. 1992). These megacrysts have homogeneous cores lacking typical compositional zoning, which makes them ideal as starting materials in experimental petrology and spectroscopic studies investigating lunar material analogs. Amma-Miyasaka and Nakagawa (2002) suggested a deep-seated plutonic body exists under the island arc, and the erupting magma entrains the anorthite megacrysts occurring on the Miyake-jima island, leading to their xenocrystic origin. It might be worth stating here that although high-anorthite megacryst occurrences are rare in general, there have been reports (Kimata et al. 1995) of other plagioclase that have An# > 90 from all over the Izu-Japan island arc system: Hachijo-jima ($An_{93.0}$), Hakone ($An_{94.3}$), Sukumogawa ($An_{93.6}$), Sukumoyama ($An_{91.4}$), Otsuki ($An_{93.0}$), Toyaba ($An_{91.3}$), Yoneyama ($An_{92.1}$), Mt. Takahara ($An_{93.8}$), Mt. Nangetsu ($An_{90.3}$), Kayodake ($An_{90.0}$), Fugoppe ($An_{92.7}$), and Kuttara ($An_{91.5}$). These anorthite samples may also be worth considering for material analogs in future studies.

Multiple studies have identified Miyake-jima anorthites as a high-quality anorthite feldspar sample owing to its megacrystic occurrence, optical clarity, and homogeneous composition. The RRUFF Project database (https://rruff.info/) lists this specimen (RRUFF ID: R0400549) along with its major element composition, Raman, X-ray diffraction, and infrared spectra. Initial spectroscopic studies of Miyake-jima anorthite megacrysts have demonstrated the utility of Miyake anorthite as a lunar material analog (Brydges et al. 2015) owing to their highly anorthitic ($An_{87–96}$) composition (Amma-Miyasaka and Nakagawa 2002). Additionally, thermal infrared laboratory measurements of these anorthites were used to place constraints on the composition of the Moon's primary anorthositic crust as observed by the Diviner Lunar Radiometer aboard the Lunar Reconnaissance Orbiter based on the position of the Christiansen feature (CF), a known spectral feature that is related to An# (e.g., Donaldson Hanna et al. 2012, 2014). Experimental petrology studies have used pulverized Miyake-jima anorthite as a starting material that mimics lunar crustal mineralogy in their investigations of Mg-suite magmatism or lunar magma ocean crystallization (Elardo et al. 2017, 2020). Branlund and Hofmeister (2012) calculate thermal diffusivities (D) of Miyake-jima anorthites among other natural plagioclase compositions and find that D decreases with increasing An content due to increased disorder. Shocked lunar anorthites have been investigated using shocked Miyake-jima anorthite analogs to understand the effect of impacts on the anorthite structure (Boslough et al. 1986; Xie et al. 2021). The hydrogen abundance of Miyake-jima anorthite crystals has been measured (Mosenfelder et al. 2015), so they could be used as a matrix-matched secondary ion mass spectrometry (SIMS) standard for the measurement of hydrogen in lunar anorthosites (Hui et al. 2017). Miyake-jima anorthites have also been used as standards for oxygen isotope analyses of ordinary chondrites and the Itokawa asteroid (Yurimoto et al. 2011). Diffusion coefficients of Mg, Ca, and Sr have been investigated by SIMS profiling on Miyake-jima anorthite to understand the evolution of their isotopic systematics in the early solar system's history (LaTourrette and Wasserburg 1998).

Although the lunar science community has identified Miyake-jima anorthites as a material analog for the FAN crust, no known study currently focuses on the natural material's detailed geochemistry. Here, we present the major, minor, and trace element concentrations of crystal fragments derived from $An_{>90}$ megacrystic anorthite, along with their intra- and intercrystalline variability. We compare our results with the existing geochemical data for different lunar crustal suites and discuss the relevant applications of the Miyake-jima anorthites as lunar crustal material analogs.

Methods

We performed electron microprobe, secondary ion mass spectrometry, and high-precision laser ablation ICP-MS analyses on seven colorless crystal fragments (Online Materials[1] Fig. S1) of Miyake-jima anorthite acquired from the University of Arizona Alfie Norville Gem and Mineral Museum, Tucson, Arizona, U.S.A. The anorthite crystals (MG-1–7) often occur with some mafic minerals, which were carefully removed by dry (water-free) polishing under ethanol using grinding paper of grit size 200–800 and finally with diamond powder of 3 and 1 μm size. Walker et al. (1995) show that turbidity in alkali feldspars is directly correlated to micro-textural features such as microporosity, alteration, fluid inclusion pits, and exsolution. Therefore, clear crystals, which showed exceptional optical clarity and were free of optically visible inclusions, were chosen in this study. These crystals were pressed into a mount of metallic indium to ensure they are available for future studies involving the measurement of volatile species like hydrogen. Additionally, some Miyake-jima megacrysts (Fig. 1) were crushed to particle sizes 75–125 μm and 125–250 μm and later purified by magnetically separating the anorthite megacrysts from their basaltic coating. These samples are used to conduct the near-infrared (NIR) and thermal infrared (TIR) spectral analyses of the Miyake-jima anorthites samples.

Major and minor element analyses

Major and minor elements in Miyake-jima anorthite were analyzed with a Cameca SX-100 Cameca electron probe microanalyzer (EPMA) at the Michael J. Drake Electron Microprobe Laboratory, Lunar and Planetary Laboratory at the University of Arizona. An accelerating potential of 15 kV was used for all the sample analyses. The beam current was 10 nA for Na and K and 20 nA for Si, Ti, Al, Mg, Ca, Fe, Mn, Cr, and P using a 5 μm beam size. Counting times were 10 s on peak and 10 s on background for Na and K. Counting times were 20 s on peak and 20 s on background for the remaining elements to improve the counting statistics. The combination of natural crystals and synthetic glasses used as standards were Hakone Anorthite (Al, Ca), Chromite - USNM 117075 (Cr), Rockport Fayalite (Fe), Orthoclase OR-1 (K Si), San Carlos Olivine (Mg), Rhodonite 104791 (Mn), Crete Albite (Na), Synthetic fluorapatite (P), and Natural Rutile (Ti). PAP correction procedures were used to convert specimen/standard intensity

Figure 1. Miyake-jima anorthite megacrysts. On the left are the intact megacrysts, highlighting their basaltic coating. On the right are crushed megacrysts showing the clear crystal cores of the sample. (Color online.)

ratios into concentrations (Pouchou and Pichoir 1991). Compositions of electron microprobe standards are listed in Online Materials[1] Table S1, and individual microprobe measurements are reported in Online Materials[1] Table S3.

Trace elements

Core to rim analyses of the Miyake-jima anorthite crystals for trace element data were collected using laser ablation inductively coupled plasma mass spectroscopy (LA-ICP-MS) and secondary ion mass spectrometry (SIMS) techniques.

Laser ablation inductively coupled plasma mass spectrometry (LA-ICP-MS). Trace element analysis on the anorthite crystals was performed by LA-ICP-MS. Analyses were performed at the METAL Core Facility, Arizona State University, using an ESI NWR193^{UC} Excimer ArF Laser Ablation system (Günther et al. 1997) attached to Thermo iCAP-Q ICP-MS. ActiveView software for the laser was coupled by way of bidirectional ethernet communication with the mass spectrometer software, Qtegra, using the relevant plugin. This ensured that the sequence timing, laser log files, and sample identification were managed automatically to facilitate subsequent data reduction in Iolite IV (Woodhead et al. 2007; Paton et al. 2011; Pettke et al. 2012). The mass spectrometer was calibrated in solution mode to establish detector cross-calibration factors and define the mass calibration. Forward power was set to 1500 W with gas flows and lens tuning parameters to optimize signal stability and minimize polyatomic species ($^{232}Th^{16}O$ acting as the main proxy). To reduce the tuning complexity, we followed the normalized argon index described by Fietzke and Frische (2016) to efficiently identify a robust tuning condition balanced against sensitivity to yield adequate counting statistics on the most trace analytes during analytical sessions. The fluence of the laser was kept at 60% (~2 J/cm^2). The gas flow of the laser carrier and nebulizer were set at 0.6 L He/min and 0.77 L Ar/min, respectively. Wash-in and wash-out times were intentionally asymmetric to improve workflow automation when selecting signal vs. gas blank in the partially automated data reduction run in Iolite IV.

Trace elements and their isotopes analyzed in four LA-ICP-MS sessions are described in Table 1, where the later sessions were used to target elements of low abundance in the anorthite crystals. Most trace elements were analyzed in the first session on the seven selected grains from edge to edge with a spot size of 50 μm, 30 Hz laser firing rate, and 4 μm/s scan speed for ~75 μm long lines. These lines were set up to closely follow the profiles analyzed in the electron microprobe. Pre-ablation scans were performed with a spot size of 55 μm, 15 Hz laser firing rate, and 30 μm/s scan speed to clean the topmost surface layer. The large spot size and lines were used to optimize the accuracy of the data and investigate both the inter- and intra-crystalline compositional heterogeneity among different Miyake-jima anorthite crystals. Low-abundance elements like HREEs and Th were analyzed in separate sessions. Therefore, the indium mount with anorthite crystals was re-polished until the ablation pits from previous sessions were no longer visible. New line patterns were laid out, so the regions analyzed directly underlay the previous ablation pits. HREEs (Gd–Lu) and Th were analyzed in Sessions II–IV listed in Table 1. Experimental conditions for the low-abundance analytes were chosen with a larger spot size of 120 μm, a 35 Hz laser firing rate, and 4 μm/s scan speed for lines ranging from 630–100 μm in length. Pre-ablation scans in Sessions II–IV were performed with a spot size of 135 μm, 35 Hz laser firing rate, and 40 μm/s scan speed.

Table 1. Dwell times in seconds of isotopes measured in the four LA-ICP-MS sessions

Session I		Session I		Session II		Session III		Session IV	
Mass	Dwell times	Mass	Dwell times	Mass	Dwell times	Mass	Dwell times	Mass	Dwell times
^{44}Ca	0.01	^{141}Pr	0.01	^{139}La	0.01	^{139}La	0.01	^{139}La	0.01
^{49}Ti	0.015	^{146}Nd	0.01	^{147}Sm	0.12	^{175}Lu	0.4	^{169}Tm	0.3
^{51}V	0.01	^{147}Sm	0.01	^{157}Gd	0.06	^{232}Th	0.1	^{174}Yb	0.3
^{52}Cr	0.01	^{153}Eu	0.01	^{159}Tb	0.02	^{238}U	0.01	^{175}Lu	0.3
^{55}Mn	0.01	^{157}Gd	0.01	^{163}Dy	0.06	$^{232}Th^{16}O$	0.01	^{232}Th	0.01
^{59}Co	0.01	^{159}Tb	0.01	^{165}Ho	0.02			^{238}U	0.01
^{63}Cu	0.01	^{163}Dy	0.01	^{166}Er	0.06			$^{232}Th^{16}O$	0.01
^{64}Zn	0.01	^{165}Ho	0.01	^{232}Th	0.01				
^{65}Cu	0.01	^{166}Er	0.01	^{238}U	0.01				
^{85}Rb	0.015	^{169}Tm	0.01	$^{232}Th^{16}O$	0.01				
^{88}Sr	0.015	^{174}Yb	0.01						
^{89}Y	0.01	^{175}Lu	0.01						
^{90}Zr	0.015	^{180}Hf	0.015						
^{93}Nb	0.01	^{208}Pb	0.01						
^{138}Ba	0.01	^{232}Th	0.01						
^{139}La	0.015	^{238}U	0.01						
^{140}Ce	0.010	$^{232}Th^{16}O$	0.01						

Note: ^{44}Ca and ^{139}La have been used as the internal standard for sessions I and II–IV, respectively.

The isotopic analyses were manually screened in the Iolite IV software for spikes in Rb, a proxy element that indicates the presence of melt inclusions, to ensure reliable (accurate and precise) analysis. The data was carefully surveyed using the Iolite software to note obvious Rb spikes compared to the general concentration in Miyake-jima crystals. Signals bearing such fluctuations or spikes were either partially or completely removed (depending on the spatial extent of the spikes) to ensure that melt inclusions were not. The NIST SRM 600 series glasses were used as the bracketing standards, and tuning was optimized with glass that had comparable (by order of magnitude) analyte concentrations for most elements. The analytical sensitivities were evaluated by comparing integrated counts in low-concentration samples and standards with blanks; where prudent, some analytes had increased dwell time to improve counting statistics in the Qtegra software running the quadrupole ICP-MS. The internal standardization in Session I was achieved by analysis of calcium in the anorthite crystals from electron microprobe (Table 2). The choice of calcium as the internal standard hinged on: (1) its high abundance (13.83–13.97%) and homogeneity within the Miyake-jima anorthite crystal cores and, furthermore, (2) calcium provides the opportunity for comparing our results to the external reference materials BCR-2G and BHVO-2G (Gao et al. 2002), which were also analyzed using the same internal standard. In Sessions II–IV, lanthanum (La) served as the internal standard because of its: (1) high abundance (0.0216–0.0290 ppm) relative to trace elements measured in Sessions II–IV; (2) homogeneity, as discussed in the results section of this study; (3) lack of polyatomic interferences (May and Wiedmeyer 1998); and (4) proximity to the analytes, HREEs and Th, in terms of the masses analyzed. The consistently flat profiles obtained for La with low standard deviations from Session I provided the rationale for using it to measure sub-parts per billion concentrations of HREEs and Th. Furthermore, when used as the internal standard, La removed the need for the electromagnet to sweep across a large range of masses as would have been the case if Ca was employed as the internal standard instead; this allowed us to obtain increased dwell times and therefore enhanced counts on the low-abundance target analytes.

Two relatively abundant copper isotopes, ^{63}Cu and ^{65}Cu, were analyzed to check for interference between ^{63}Cu and $^{23}Na^{40}Ar$. Oxide (Th/ThO) production rates were monitored and observed to be <1% throughout the analytical session, which is also an indicator of robust plasma conditions balancing the signal-to-noise ratio for the analytes while keeping polyatomic species relatively low. The robust plasma conditions facilitate analysis of non-matrix-matched calibration and bracketing standards for LA-ICP-MS signals (e.g., Heinrich et al. 2003). Though imperfect, the NIST SRM 600 series glass standards provided the best available material for calibration, having similar ablation thresholds and concentration ranges for many analytes. Moreover, our selected standards allowed suitably accurate results for external standards, as described below.

Data reduction was performed using Iolite software with the "Trace Elements Next" Data Reduction Scheme (DRS). Where possible, automatic selections were employed for the baseline and sample region to maintain objectivity. All time-series traces were carefully inspected for anomalies such as melt inclusions (described above). The accuracy of measurements during Session I was tested by measurement of external standard BCR-2G and BHVO-2G between every 3–4 analyses. The measured concentrations from the external standards have been compared with the values reported by Gao et al. (2002) with LA-ICP-MS (Online Materials[1] Fig. S2). Based on a total of 24 BCR-2G and BHVO-2G measurements on external standards recorded during Session I, the relative errors (Gao et al. 2002) for the trace elements are approximately within the 20% for BCR-2G and 25% for BHVO-2G (Online Materials[1] Fig. S2). The 1σ standard deviation error bars represent the reproducibility of the analyses during Session I, which is <9%. Individual analyses of BCR-2G and BHVO-2G external reference material are reported in Online Materials[1] Table S2. The two copper isotopes, ^{63}Cu and ^{65}Cu, display good agreement among the natural anorthite samples, with the slope approximating 1 and an intercept close to the origin (Online Materials[1] Fig. S3). This established that there is negligible interference between ^{63}Cu and $^{23}Na^{40}Ar$.

Secondary ion mass spectrometry. Depth profiles of minor and trace elements Na, K, Ti, and Li were measured using the Ametek Cameca IMS6f SIMS at the NSF National Facility at Arizona State University. A primary beam of O_2^- was accelerated to 12.5 keV, focused to a spot, and rastered over a 20 × 20 μm^2 area to sputter a flat crater. A 400 μm field aperture allowed ions from a 15 μm diameter circular area in the center of the sputtered crater into the mass spectrometer, eliminating ions derived from the crater walls. Positive secondary ions were accelerated to 9000 eV. The following ion intensities were collected: ^7Li, ^{23}Na, ^{39}K, ^{47}Ti, and ^{30}Si. All secondary ion signals were normalized to the count rate for $^{30}Si^+$, a matrix ion. Secondary ions were examined with 0 ± 20 eV energy, and no energy filtering was applied. The primary beam current was ~5 nA, and the pressure in the analytical chamber varied from 1.13×10^{-9} to 0.75×10^{-9} torr over the analytical session.

The sample was pre-sputtered for 180 s at the beginning of each analysis to lower the probability of analyzing K present as surface contamination. Interference between ^{39}K and $^{23}Na^{16}O$ was resolved by closing the entrance and exit slits of the mass spectrometer to cleanly separate these two species ($M/\Delta M < 2000$). Any interferences on Ti were also resolved at this mass resolving power. Note that the abundant ^{48}Ti isotope was not used because of the unresolvable interference from ^{48}Ca. A single cycle took ~11 s, including waiting time, to settle the magnetic field at each mass. Peaks for each of the different isotopes were detected by either the electron multiplier (EM) or Faraday Cup (FC) secondary ion detectors in the following order: ^7Li (1 s, EM), ^{23}Na (1 s, FC), ^{39}K (2 s, FC), ^{47}Ti (1 s, EM), and ^{30}Si (1 s, EM). NIST series glasses -610, -612, -614, -620, and GSE were used to calibrate the Li, Na, K, and Ti concentrations in anorthite. Throughout the analyses, charge was compensated by moving the magnetic field to detect ^{30}Si, and the sample voltage was ramped from 8901 to 8801 V every fifth cycle. The sample voltage was placed at the centroid of the voltage vs. secondary ion intensity curve. The charge compensation routine was similar to the process described in Shamloo et al. (2021). The largest 2σ standard errors for the ion ratios recorded are $^7Li/^{30}Si$ (2.8%), $^{23}Na/^{30}Si$ (0.36%), $^{39}K/^{30}Si$ (1.42%), and $^{47}Ti/^{30}Si$ (1.88%).

Near- and thermal infrared spectroscopy

We acquired near-infrared (NIR) reflectance and thermal infrared (TIR) emissivity measurements within the Planetary Spectroscopy Facility at the University of Oxford. Miyake-jima megacrysts coated in basalt were initially crushed and sieved into size fractions of 75–125 and 125–250 μm and washed with distilled water for magnetic separation. Anorthite megacryst materials were separated from their basaltic coating and mafic inclusions by putting each particle size fraction through a Frantz magnetic separator. Each particle size fraction was run through the Frantz at least three times until only the anorthite particles remained in the non-magnetic fraction as determined in a microscope. Once magnetically separated, the sample was further crushed and sieved into <25 and 125–250 μm particle size fractions. The 125–250 μm particle size fraction was used for near-infrared reflectance measurements as this particle size fraction is ideal for highlighting diagnostic spectral features in the NIR, while the <25 μm particle size fraction was used for thermal infrared emissivity measurements as it is the spectrally dominant particle size at TIR wavelengths.

NIR reflectance measurements were made using a Brüker IFS 66v Fourier Transform Infrared (FTIR) spectrometer with a Specac Diffuse Reflectance FTIR Accessory, a CaF_2 beamsplitter and a deuterated triglycine sulfate (DTGS)

Table 2. Electron microprobe compositions in wt% of Miyake-jima anorthites cores and rims

Sample	(n)	SiO_2	Al_2O_3	CaO	Na_2O	MgO	FeO	Total	An#
Core MG-1	22	43.68(16)	35.73(19)	19.41(10)	0.47(5)	0.08(1)	0.44(3)	99.8(26)	95.79(48)
Core MG-2	36	43.67(16)	35.5(16)	19.4(9)	0.52(6)	0.08(1)	0.46(3)	99.64(16)	95.4(51)
Core MG-3	41	43.6(16)	35.77(17)	19.54(11)	0.43(9)	0.08(1)	0.42(3)	99.83(20)	96.09(54)
Core MG-4	33	43.75(20)	35.84(15)	19.42(9)	0.48(3)	0.08(1)	0.43(3)	100.01(27)	95.72(29)
Core MG-5	27	43.82(20)	35.61(17)	19.35(11)	0.54(5)	0.09(1)	0.45(3)	99.86(27)	95.22(43)
Core MG-6	68	43.76(13)	35.62(14)	19.4(8)	0.52(4)	0.08(2)	0.48(4)	99.85(21)	95.38(39)
Core MG-7	75	43.71(12)	35.63(14)	19.36(6)	0.5(10)	0.08(1)	0.46(4)	99.74(21)	95.39(42)
Rim MG-4	1	46.01	34.08	17.98	1.44	0.15	0.67	100.32	87.32
Rim MG-7	1	46.15	33.33	17.35	1.55	0.13	0.99	99.49	86.1

Notes: Anorthite (An#) has been calculated from 8 oxygen cation normalization. The wt% errors (in parentheses) are the 1σ standard deviation from the mean with the least unit cited. Ti, Mn, Cr, P, and K measurements with the microprobe were consistently below the detection limits of the individual elements and have not been reported. n is the average number of analyses for different grains' core domains.

detector. The measurements were taken at a resolution of 2 cm^{-1} from ~0.8 to 5 μm using a 12 mm aperture, 2.2 kHz scanner velocity, and 125 scans. TIR emissivity measurements were made under ambient ("Earth-like") and simulated lunar environment (SLE) conditions using the Planetary Analogue Surface Chamber for Asteroid and Lunar Environment (PASCALE) chamber (Donaldson Hanna et al. 2021). PASCALE is mounted to the emission port of a Bruker VERTEX 70v FTIR spectrometer using a cesium iodide (CsI) window. Thermal infrared spectra were measured at a resolution of 4 cm^{-1} from ~2400 to 200 cm^{-1} (~5 to 50 μm) using a wide-range TIR beamsplitter and a deuterated, L-alanine doped triglycine sulfate (DLaTGS) detector. Three measurements of 250 scans were made of each sample, producing a spectrum with sufficient signal-to-noise so we can uniquely identify features of 2% contrast from the noise. The final TIR spectrum for each sample is an average that has been calibrated using published methods (e.g., Ruff et al. 1997) and spectral measurements of a calibration target painted with Nextel high-emissivity black paint at 340 and 360 K (e.g., Thomas et al. 2012). The near-surface conditions of the lunar regolith are simulated by creating thermal gradients similar to those experienced on the Moon. Thermal gradients are created in the uppermost position of the lunar soils by evacuating the chamber to vacuum pressures ($<10^{-4}$ mbar), cooling the interior of the chamber to <125 K using liquid nitrogen (LN_2), and then heating the samples from below and above to brightness temperatures similar to those on the Moon (e.g., Donaldson Hanna et al. 2017; Williams et al. 2017).

Results

We present the chemical data of the Miyake-jima crystals obtained from the analytical instruments employed in this study: electron microprobe, LA-ICP-MS, and SIMS. This section focuses on the crystal core compositions and intra- and inter-crystalline heterogeneity. It highlights the reproducibility of elemental data across the different analytical techniques applied to the Miyake-jima sample suite.

Variability of mineral chemistry

We employ all three analytical techniques—electron microprobe, LA-ICP-MS, and SIMS—to investigate the variability of major, minor, and trace chemical composition within individual anorthite crystals and across the sample set.

Major and minor elements. Table 2 lists the average electron microprobe analyses of cores and rims of each Miyake-jima grain chosen in this study. Individual analyses across the profiles (shown in Fig. 2) are listed in the Online Materials[1] Table S3. MG-4 and MG-7 show distinct bytownite ($An_{86–87}$) margins of ~25 μm surrounding the homogeneous core. Calculations of anorthite composition do not include the K-feldspar end-member because K is present only in trace quantities. Figure 2 shows that SiO_2 and Al_2O_3 wt% vary stoichiometrically near the bytownitic rims: SiO_2 increases from ~44 to ~46%, and Al_2O_3 decreases from ~36 to ~33%. The high-albite margins of MG-4 and MG-7 exhibit more drastic fluctuations in MgO (an increase from ~0.08 to ~0.14%) and FeO (increases from ~0.43 to ~0.85%), also seen in Figure 2. Measurements of other elements (Ti, Mn, Cr, K, and P) were consistently below their respective EPMA detection limits. The approximate detection limits of the electron microprobe analyses are: Ti 220 ppm, Mn 500 ppm, Cr 230 ppm, K 350 ppm, and P 300 ppm.

Trace elements. SIMS analyses show that the bytownitic rims contrast with the cores in trace and major element compositions. As seen in Figure 3, with respect to the core, the rims are enriched in Li (by 1.5–3.5 times), K (by 1.2–2.4 times), Na (by ~1.7 times), and Ti (by 1.1–1.2 times). It must be noted that the true bytownite rim may have been only partially captured in MG-4 and MG-7 during SIMS analysis due to the lack of optical differences between the domains. Other crystals chosen in this study lacked any distinctly heterogeneous margin and reflect the heterogeneity in the cores of Miyake-jima anorthites. Li, K, Na, and Ti concentrations with 1σ errors for the cores of the seven Miyake-jima grains are 0.31 ± 0.14 ppm, 44.01 ± 3.77 ppm, 3510 ± 461 ppm, and 37.29 ± 2.93 ppm, respectively, for the calibration constructed with the both GSE and NIST-series glasses. Table 3 summarizes the trace element concentrations derived from 14 SIMS analyses performed on the Miyake-jima anorthite grains. Individual SIMS analyses are in Online Materials[1] Table S4.

LA-ICP-MS analyses were unable to analyze the rims of the Miyake-jima crystals due to the larger spot size (135 μm) of analyses compared to the narrow rims (<25 μm) of the anorthites. Therefore, the trace element data derived from the ICP-MS is directed toward exploring the inter-crystalline heterogeneity and/or homogeneity of individual crystal cores. Trace element data for grain domains collected over all ICP-MS sessions are compiled in Table 4. Individual trace element analyses from all LA-ICP-MS sessions are reported in Online Materials[1] Table S2. In Table 5, we report the summative average major, minor, and trace element composition of all Miyake-jima anorthites crystals analyzed in this study.

For illustrative purposes, Figure 4 shows the profile of two grains, MG-4 and -7, which had distinct rims observed in terms of major elements. The profiles for the other grains are in Online Materials[1] Figure S4. MG-4 shows a prominent enrichment of all LREEs by about one order of magnitude toward the margin. The profile for MG-7 could not capture the "true" rim of the grain, possibly because the large laser spot likely overlapped onto the more homogeneous crystal interior. Table 6 shows the 1σ percentage standard deviations for each LREE measured for cores of all Miyake-jima samples in the LA-ICP-MS. The largest standard deviation recorded is 30.91, with most percent standard deviations being within 10–20%, showing that the LREEs are homogeneously distributed in the cores of the Miyake-jima anorthites. The intercrystalline homogeneity is also evident from Figure 4 and Online Materials[1] Figure S4.

Thorium concentrations were below detection limits in all LA-ICP-MS sessions except for a few analyses in Session IV. The increased dwell time from 0.01 to 0.10 s on ^{232}Th in Session IV helped improve the sensitivity for thorium measurements (see Online Materials[1] Fig. S5). It may be noted that detection limits improve (i.e., decrease) from Session I to Session IV as a result of increased effective dwell times on thorium and thus improved sensitivity. Thorium has been measured above the limits of detection (LODs; calculated according to Pettke et al. 2012) for only MG-2 and -7 in Session IV. However, the thorium concentrations for MG-2 have lower confidence because their 2σ uncertainties overlap the LODs. The best thorium analyses above detection limits with 2σ errors are from MG-7: 0.122 ± 0.035, 0.026 ± 0.015, and 0.015 ± 0.010 ppb.

NIR and TIR spectral measurements

The NIR reflectance measurement of the 125–250 μm particle size fraction confirms the crystalline nature of the Miyake-jima anorthite megacrysts as it has a distinct absorption band near 1.25 μm due to minor amounts of Fe^{2+} in the crystal

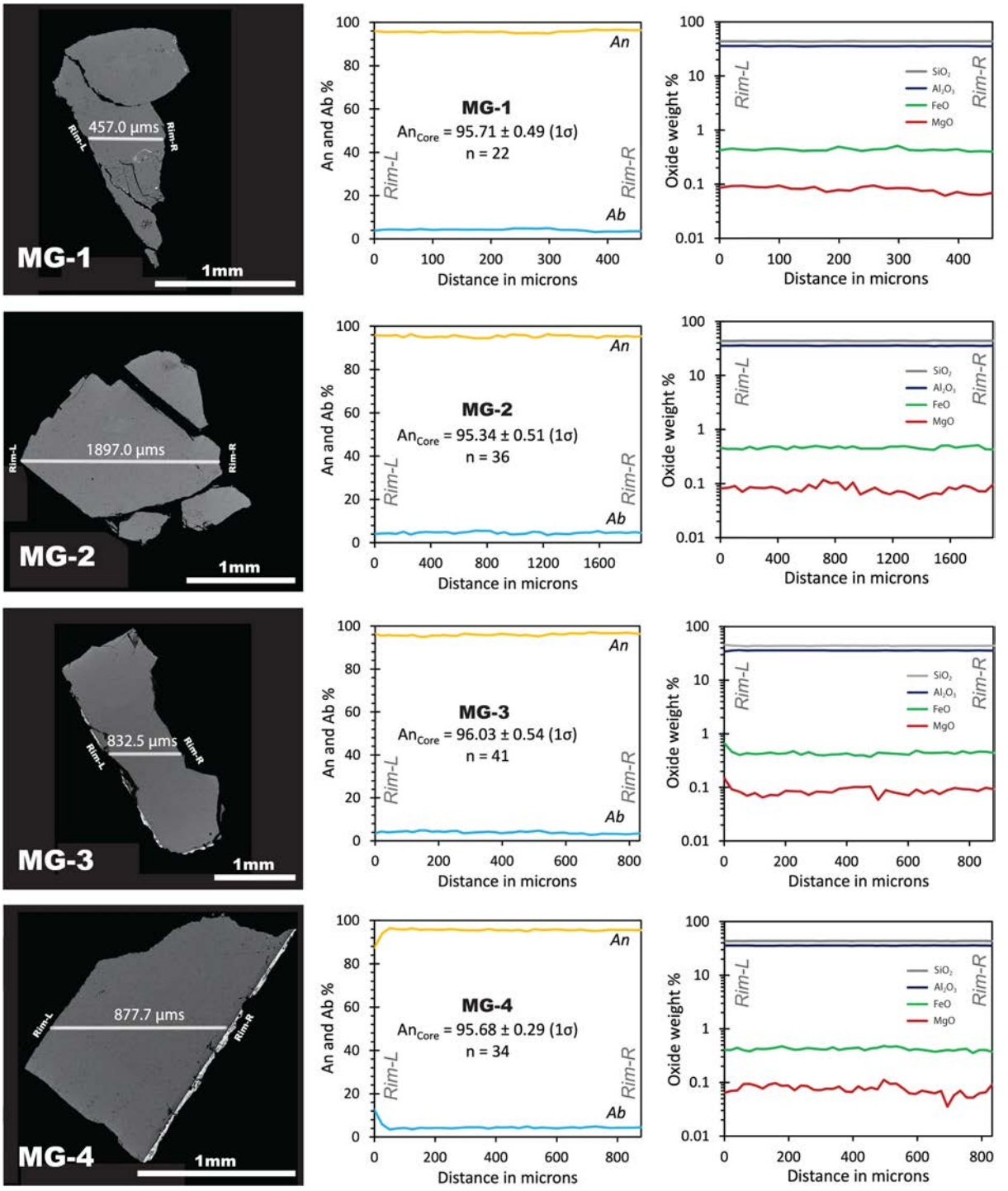

Figure 2. Backscattered electron (BSE) images of Miyake-jima Grains (MG-1–7). The microprobe compositional variation between anorthite–albite (An-Ab) and major elements (SiO_2, Al_2O_3, FeO, and MgO) are shown across the profile marked (as Rim-L to Rim-R) in the corresponding BSE images. One-sigma standard deviations of mean anorthite concentration have been reported for the cores of each crystal fragment. (Color online.)

structure (see Fig. 5). The lack of NIR diagnostic absorption bands near 1.0 and 2.0 µm demonstrates that the basaltic coating and mafic inclusions have been effectively removed and the sample is composed entirely of the anorthite core crystal material. At these wavelengths, the spectra of other terrestrial anorthites are often affected by the Earth's weathering process that acts to remove the diagnostic absorption feature near 1.25 µm and introduce additional features from accessory

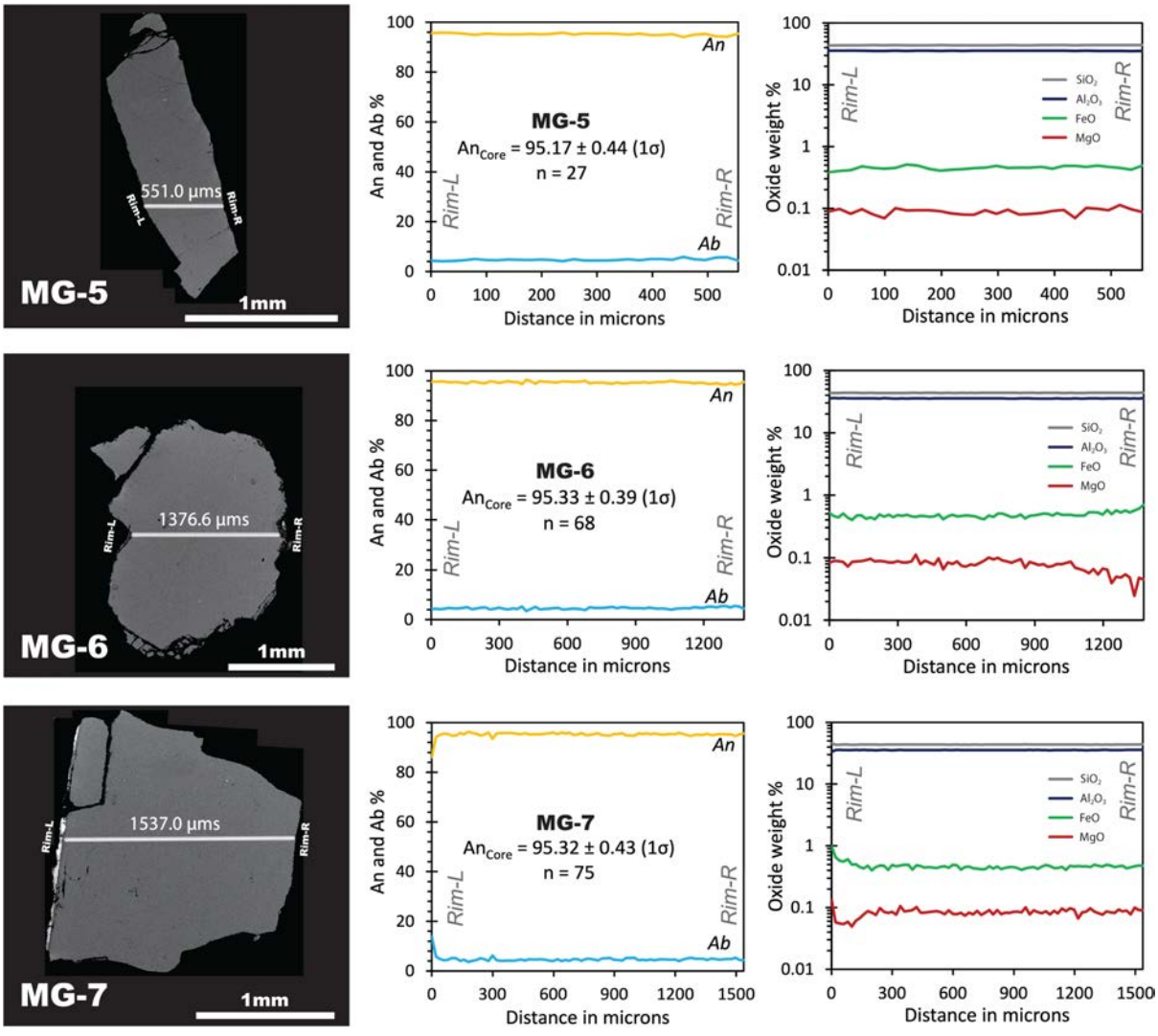

FIGURE 2.—*CONTINUED.*

minerals complicating the spectral signature (e.g., Adams and Goullaud 1978). The TIR emissivity measurements made under ambient and simulated lunar environment (SLE) conditions of the <25 µm particle size fraction have spectral features consistent with highly calcic plagioclase. Specifically, the Christiansen feature (CF) positions identified in the ambient and SLE spectra of Miyake-jima anorthite (1233.9 and 1275.6 cm^{-1}, respectively) are similar to terrestrial anorthites previously measured in the lab (e.g., Nash and Salisbury 1991; Milam et al. 2004; Donaldson Hanna et al. 2012, 2014). However, we observe differences between the Miyake-jima anorthite spectra and previously published terrestrial anorthite spectra. Specifically, we find that the position of spectral features, including the transparency feature (TF) and vibration bands, are at lower frequencies (longer wavelengths) than previously measured terrestrial anorthite spectra that are less calcic than the Miyake-jima anorthites. Additionally, we observe: (1) that the shape of these spectral features is more distinct (less rounded) and (2) weaker vibration band features (spectral contrasts 3%) that were not previously identified in lab spectra of terrestrial anorthites, both which could result from the crystalline nature of the Miyake-jima anorthites and/or the improved spectral resolution of our laboratory measurements. Finally, similar to the NIR measurements, no spectral features are observed in the TIR spectra owing to the basaltic coating and mafic inclusions.

Comparison of analytical techniques

The precision and accuracy of Ti and Na were independently examined by comparing the results obtained from the electron microprobe, LA-ICP-MS, and SIMS analytical techniques. Online Materials[1] Figure S6 shows the Ti and Na ppm concentrations measured for the cores of the seven selected grains. The 1σ errors on the microprobe measurements of the Na in the cores are considerably larger than the more precise SIMS estimations for Na. The electron microprobe analyses on Online Materials[1] Figure S6a were chosen carefully to spatially overlap with the area rastered by the SIMS analysis. Although in close proximity, it may be noted that the points shown in Online Materials[1]

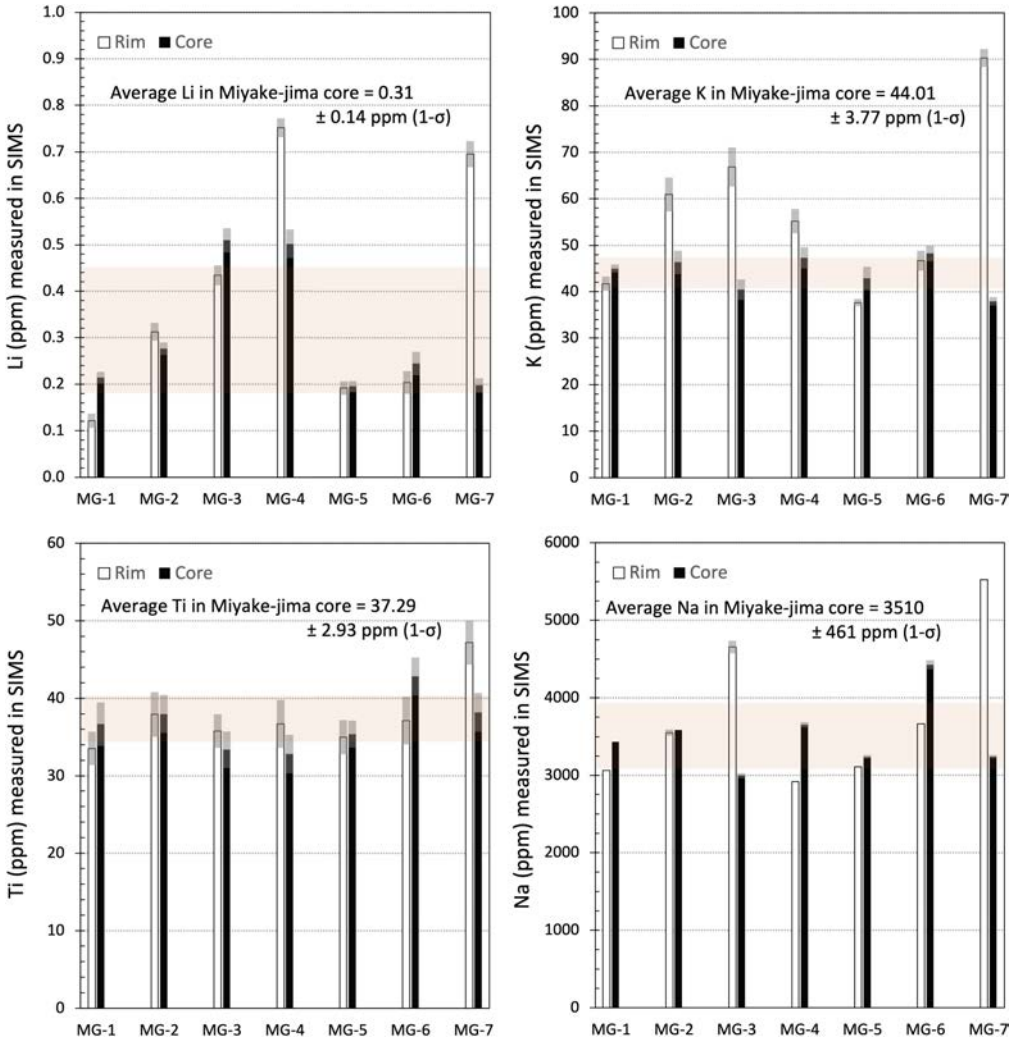

Figure 3. Variation in Li, K, Ti, and Na (ppm) as measured by individual SIMS spot analyses. Pairs of cores (black bars) and rims (white bars) from the same Miyake-jima crystal indicate the intra-granular chemical variability in Li, K, Na, and Ti. One-sigma standard errors from individual SIMS analytical spots are shown as gray bars. The shaded region depicts the average and 1σ standard deviation of the population of the core. Note that only MG-4 and MG-7 sample the albitic rim, while other crystals show heterogeneity in the core. (Color online.)

Figure S6a do not have a volumetric overlap since the sample excitation volume for the electron microprobe is much smaller than the volume sputtered by the ion microprobe. The comparison between the different analytical techniques collectively reflects the volumetric heterogeneity within individual anorthite crystal cores and the effect of different instrumental and analytical parameters. The intra- and inter-crystalline heterogeneity for Na is high because their concentrations vary by ~1500 ppm (based on SIMS and EPMA) and plot on either side of the 1:1 line (Online Materials[1] Fig. S6b). The Ti concentrations derived from individual SIMS analyses are systematically underestimated compared to the LA-ICP-MS measurements by a factor of 0.78–0.94. For Ti, the 1σ standard deviation of the population from multiple LA-ICP-MS measurements is comparable with the seven individual SIMS analyses of the seven Miyake-jima grain cores. A reduction in the systematic errors is noted in Online Materials[1] Figure S6b for the Ti concentrations derived from SIMS when calibrated against only GSE glasses, in contrast to a combination of GSE and NIST-series glasses. We note an improvement of the correlation factor (slope in Online Materials[1] Fig. S6b) from 0.88 to 0.99 when using the

Table 3. Trace element concentrations (in ppm) of Miyake-jima anorthites grain cores and rims from SIMS analyses

Sample	Li	Na	K	Ti
MG-1 core	0.2141(3)	3434.5(77)	44.94(2)	36.66(6)
MG-1 rim	0.1216(4)	3065.04(58)	41.67(3)	33.54(5)
MG-2 core	0.2765(3)	3586.11(78)	46.31(6)	37.98(6)
MG-2 rim	0.3126(4)	3550.97(28)	60.95(8)	37.93(7)
MG-3 core	0.5099(6)	2997.38(55)	40.41(5)	33.37(5)
MG-3 rim	0.4343(5)	4655.57(112)	66.86(9)	35.77(5)
MG-4 core	0.752(7)	3652.3(133)	55.22(5)	36.72(7)
MG-4 rim	0.5018(5)	2921.05(89)	47.27(6)	32.82(6)
MG-5 core	0.1952(3)	3237.25(54)	42.9(6)	35.34(4)
MG-5 rim	0.1918(3)	3108.42(23)	37.69(2)	34.97(5)
MG-6 core	0.2451(6)	4424.55(107)	48.27(4)	42.81(6)
MG-6 rim	0.2042(6)	3664.27(92)	46.71(5)	37.11(7)
MG-7 core	0.1973(4)	3240.52(88)	37.98(2)	38.17(6)
MG-7 rim	0.6952(6)	5525.25(175)	90.3(4)	47.16(6)

Note: The errors are reported as 1σ standard errors of the mean.

Table 4. LA-ICP-MS trace element composition in ppm of average Miyake-jima anorthite cores and single raster analyses of the rims in MG-4 and MG-7

	MG-1 core	MG-2 core	MG-3 core	MG-4 core	MG-5 core	MG-6 core	MG-7 core	MG-4 rim	MG-7 rim
Ti	38.8(33)	49.9(151)	37.4(32)	66.0(25)	45.0(23)	45.4(21)	43.0(19)	375.1(70)	43.5(11)
V	1.12(9)	1.31(83)	1.09(8)	0.94(3)	1.04(6)	1.20(6)	1.12(6)	8.03(21)	1.13(5)
Cr	0.71(9)	0.73(56)	0.73(27)	0.53(6)	0.58(14)	0.71(11)	0.67(19)	4.42(73)	0.69(10)
Mn	22.7(4)	23.7(31)	22.8(4)	21.2(4)	22.3(3)	24.1(36)	22.4(10)	183.2(13)	32.9(4)
Co	0.32(4)	0.32(7)	0.33(4)	0.29(2)	0.33(4)	0.31(3)	0.32(3)	2.45(15)	0.26(2)
Cu^{63}	1.00(19)	0.95(15)	2.16(86)	2.02(44)	1.00(9)	1.15(36)	1.21(36)	10.27(38)	2.49(9)
Zn	1.24(15)	1.36(31)	1.22(27)	1.00(9)	1.31(9)	1.36(13)	1.26(14)	9.00(53)	1.51(11)
Cu^{65}	0.90(18)	1.45(207)	2.08(89)	2.08(41)	0.97(13)	1.14(34)	1.19(39)	10.6(7)	2.56(13)
Ba	5.45(21)	5.99(34)	5.18(32)	5.14(13)	5.76(24)	5.80(19)	5.50(13)	2806(14)	299.4(22)
Sr	309.1(35)	326.2(62)	310.9(97)	319.8(25)	325.4(44)	320.3(39)	323.3(43)	0.3(1)	0.06(1)
Nd	0.05(1)	0.06(2)	0.06(1)	0.05(1)	0.06(1)	0.05(1)	0.06(1)	44.14(49)	6.26(9)
La	0.027(3)	0.033(6)	0.028(4)	0.030(3)	0.033(5)	0.032(4)	0.031(4)	0.270(3)	0.030(1)
Ce	0.06(1)	0.07(1)	0.06(1)	0.06(1)	0.07(1)	0.07(1)	0.06(1)	0.51(4)	0.08(1)
Pr	0.010(2)	0.011(3)	0.011(3)	0.010(1)	0.011(2)	0.011(2)	0.011(3)	0.093(17)	0.009(2)
Nd	0.05(1)	0.06(2)	0.06(1)	0.05(1)	0.06(1)	0.05(1)	0.06(1)	0.48(9)	0.08(2)
Sm[a]	0.011(2)	0.012(1)	0.015(2)	0.015(2)	0.011	0.015(1)	0.013(2)	<d.l.	<d.l.
Eu	0.064(10)	0.068(7)	0.057(13)	0.062(7)	0.069(5)	0.063(7)	0.063(7)	0.550(5)	0.070(1)
Gd[a]	0.0105(0)	0.0108(8)	0.0147(20)	0.0128(14)	0.0095	0.0135(14)	0.0123(24)	<d.l.	<d.l.
Tb[a]	0.0020(2)	0.0013(2)	0.0016(2)	0.0018(4)	0.0014	0.0017(2)	0.0015(4)	<d.l.	<d.l.
Dy[a]	0.0086(34)	0.0068(4)	0.0097(12)	0.0082(13)	0.0050	0.0089(9)	0.0079(14)	<d.l.	<d.l.
Ho[a]	0.0015(11)	0.0012(1)	0.0016(3)	0.0015(3)	0.0010	0.0014(2)	0.0014(4)	<d.l.	<d.l.
Er[a]	0.0036(21)	0.0026(3)	0.0035(6)	0.0031(9)	0.0027	0.0033(5)	0.0030(9)	<d.l.	<d.l.
Tm[a]	0.00034(16)	0.00029(4)	0.00027(4)	0.00030(8)	0.00031	0.00029(3)	0.00029(6)	<d.l.	<d.l.
Yb[a]	0.0020(6)	0.0018(3)	0.0016(3)	0.0016(2)	0.0020	0.0017(2)	0.0017(3)	<d.l.	<d.l.
Lu[a]	0.00019(6)	0.00020(4)	0.00018(5)	0.00018(2)	0.00022(9)	0.00020(3)	0.00019(2)	<d.l.	<d.l.
Y	0.036(8)	0.055(47)	0.038(13)	0.039(4)	0.038(8)	0.042(9)	0.038(7)	<d.l.	<d.l.
Pb	0.08(3)	0.06(1)	0.19(6)	0.05(1)	0.06(2)	0.09(3)	0.10(6)	<d.l.	0.30(5)

Notes: The errors reported for the cores and rims are the 1σ standard errors of all the individual analyses averaged for each sample. <d.l. indicates analyses that were below the detection limits. Data points where uncertainties are not mentioned are single raster analyses for that sample. The number of data points averaged and individual analyses for each crystal have been reported in the Online Materials[1] Table S2.
[a] Elements for which La was used as the internal standard in sessions II–IV.

Table 5. One-sigma percent standard deviations of individual LREEs in the Miyake-jima crystal cores

Sample	# of analyses	La	Ce	Pr	Nd	Eu
MG-1	7	11.45	10.30	17.02	22.09	15.82
MG-2	28	17.45	22.17	30.91	25.04	9.88
MG-3	13	16.12	18.15	24.08	23.83	23.43
MG-4	13	9.70	8.65	11.50	19.98	10.98
MG-5	9	13.99	6.16	20.97	23.79	6.75
MG-6	23	13.55	8.63	17.56	22.60	11.36
MG-7	32	13.22	11.69	26.78	23.34	11.63

calibration with GSE glass only. The underestimation of Ti from the calibration, including NIST-series glasses, is due to the high SiO_2 content (~70%) in the NIST matrix compared to the anorthites. The matrix of the GSE glasses ($SiO_2 \approx 43.7\%$) is a better match for the anorthites ($SiO_2 \approx 43.7\%$) than the NIST matrix. The dependence of Ti ion yield on the SiO_2 matrix has been documented by Behr et al. (2011). However, measurements from both analytical techniques indicate that inter- and intra-crystalline homogeneity are high for titanium. Comparisons for Li and K are not shown here as Li was not measured by any other technique, while K was below the detection limit (~350 ppm) for the electron microprobe.

Discussion

Average core compositions across all crystals range from An# = 95.17–96.03 (Fig. 6), confirming the compositional homogeneity of the anorthite crystal cores, as reported by Amma-Miyasaka and Nakagawa (2002). Some unfragmented crystals show bytownite rims of <25 μm. These crystal margins are notably enriched in Fe, Mg, Li, Ti, K, and REEs. Within the sample suite, only MG-4 (see Fig. 4) shows a prominent enriched LREE signature in the crystal rim. Whether this feature is limited to only one sample or is characteristic of the sample suite is not clear. However, these rims are not optically distinct from the homogeneous high-An cores. Although these lower-Ca rims have been observed during microanalysis, their volume (3.8–8.3 vol%, assuming spherical geometry of the crystals) is negligible for analyses and experiments requiring a crushed sample. Prior to spectral characterization, the basaltic coatings were removed by magnetic separation, which was also confirmed by the absence of any NIR diagnostic absorption bands near 1.0 and 2.0 μm. However, since the bytownitic rims are not optically or magnetically different from the anorthite cores, they could not be identified and effectively separated. Despite this, VNIR and TIR spectral features due to minor amounts of bytownite are not observed because the bytownite rims have a minor presence (i.e., An# 85–88) and are mixed in with the more anorthitic cores. This is not surprising for two reasons: (1) at TIR wavelengths, it has been demonstrated that a material must comprise at least 5–10 vol% of a spectrally distinct material to contribute to the overall spectral signature (e.g., Ramsey and Christensen 1998), and (2) Cheek and Pieters (2014) showed that an intermediate plagioclase sample had the same VNIR band position at 1.25 μm as that of highly calcic plagioclase.

The REE patterns (Fig. 7) of the Miyake-jima anorthite grain cores chosen in this study are subchondritic and have a negative slope, meaning they are enriched in the LREEs with progressive

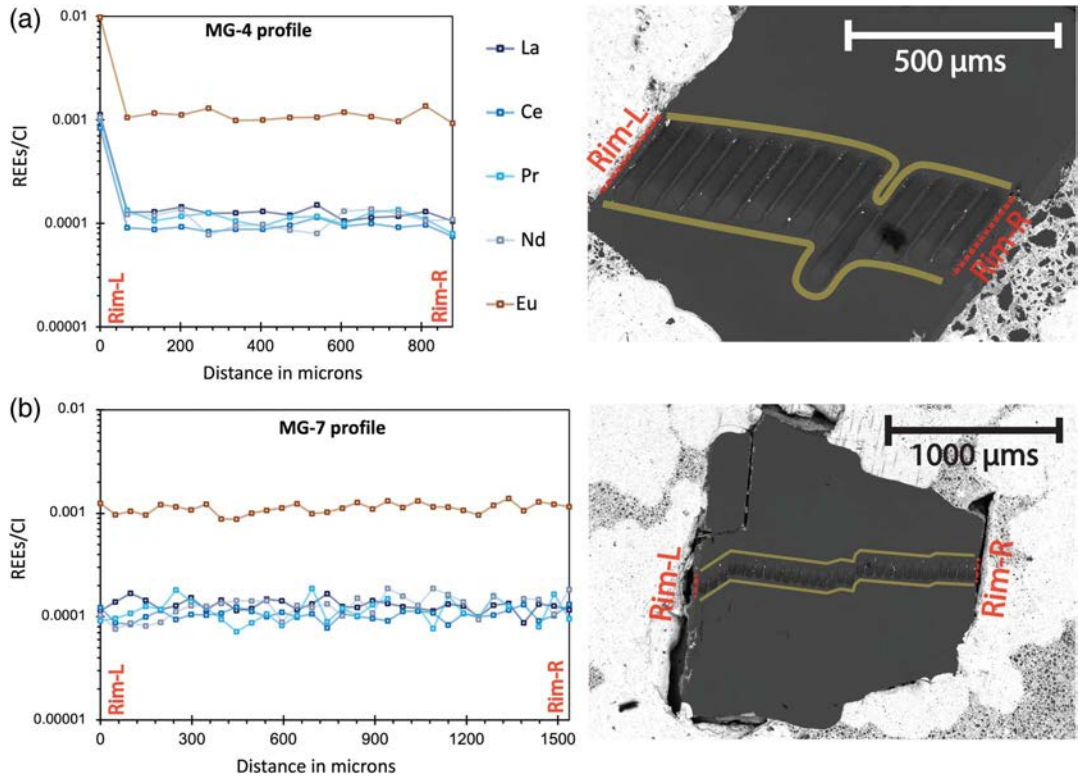

Figure 4. Chondrite-normalized (McDonough and Sun 1995) individual LREEs across profiles of crystals MG-4 and MG-7, where the distance on the x-axes represent scan steps from edge to edge of individual crystals. The corresponding BSE images show the pits formed due to ablation. These raster profiles have been reconstructed using data from "Session I," where a laser spot size of 35 µm was used to ablate raster lines of ~75 µm length. (Color online.)

HREE depletion. The homogeneous LREE distribution across the cores of Miyake-jima crystals is evident from the: (1) small 1σ percent standard deviations reported in Table 5, (2) small error bars shown in Figure 7, and (3) considerably flat individual LREE measurements across the crystal core (Fig. 4; Online Materials[1] Fig. S4). All plagioclase grains have a variable but positive Eu anomaly (Eu/Eu* = 11.7–21.1, where Eu* is the square root mean of the product of chondrite-normalized Sm

Table 6. Major, minor, and trace element concentrations of Miyake-jima anorthites grain cores from a combination of data collected from microprobe, SIMS, and LA-ICPMS analyses

Major and minor elements					
SiO_2	(wt%)	43.71(6)	Si	(wt%)	20.43(3)
Al_2O_3	(wt%)	35.67(13)	Al	(wt%)	18.88(7)
CaO	(wt%)	19.41(6)	Ca	(wt%)	13.87(4)
Na_2O	(wt%)	0.50(3)	Na	(wt%)	0.36(3)
MgO	(wt%)	0.08(1)	Mg	(wt%)	0.048(6)
FeO	(wt%)	0.45(2)	Fe	(wt%)	0.35(2)
Trace elements					
K	(ppm)	44.0(38)	Mn	(ppm)	22.77(97)
Ti	(ppm)	46.5(96)	Sr	(ppm)	319.3(68)
Ba	(ppm)	5.55(32)	Sm	(ppm)	0.013(2)
Li	(ppm)	0.32(14)	Eu	(ppm)	0.064(4)
V	(ppm)	1.12(12)	Gd	(ppm)	0.012(2)
Cr	(ppm)	0.67(8)	Tb	(ppm)	0.0016(2)
Co	(ppm)	0.32(1)	Dy	(ppm)	0.008(2)
Cu^{63}	(ppm)	1.43(48)	Ho	(ppm)	0.0014(2)
Zn	(ppm)	1.25(12)	Er	(ppm)	0.0031(4)
Cu^{65}	(ppm)	1.40(50)	Tm	(ppm)	0.0003(2)
Nd	(ppm)	0.06(1)	Yb	(ppm)	0.0018(2)
La	(ppm)	0.031(2)	Lu	(ppm)	0.00019(1)
Ce	(ppm)	0.06(1)	Y	(ppm)	0.04(1)
Pr	(ppm)	0.011(5)	Pb	(ppm)	0.09(5)
Nd	(ppm)	0.06(1)			

Note: The errors are reported as 1σ standard errors of the mean [e.g., 43.71 ± 0.06 wt% is represented as 43.71(6)].

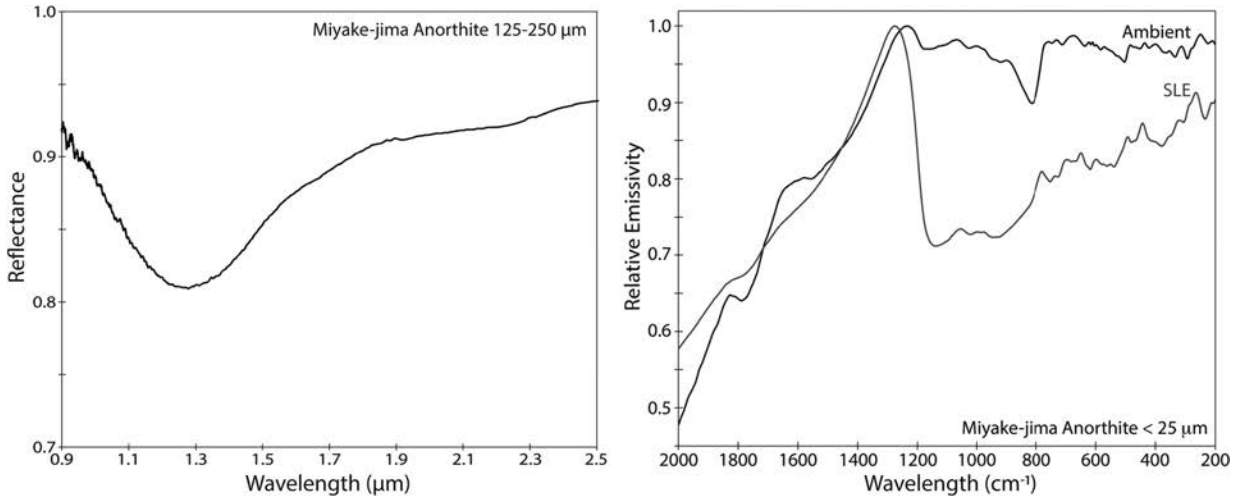

Figure 5. (Left) NIR reflectance spectrum of Miyake-jima anorthite (particle size fraction 125–250 µm) with the characteristic 1.25 µm band for crystalline plagioclase. (Right) TIR emissivity spectra of Miyake-jima anorthite (particle size fraction <25 µm) measured under ambient and simulated lunar environment (SLE) conditions.

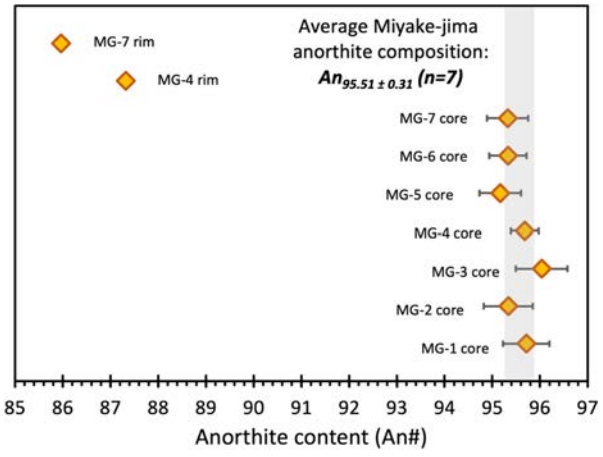

Figure 6. Average anorthite content (An#, calculated from 8 oxygen formula units) of the individual Miyake-jima grain cores with 1σ standard errors from the mean and single rim analyses from MG-4 and MG-7. The average anorthite content of the seven individual grains analyzed in this study is $An_{95.5\pm0.3}$ (1σ), represented by the shaded area. (Color online.)

and Gd). The best measurements of low-concentration thorium are 0.122–0.015 ppb, indicating its very low concentration. Murakami et al. (1991) identified crystallographically oriented native copper inclusions within the Miyake-jima lattice; however, we did not observe such inclusions in optical or electron images. There were no notable spikes or fluctuations in the signal of copper observed during the time-resolved analysis, which would correspond to the laser ablating copper inclusions.

The NIR reflectance absorption band near 1.25 µm (Fig. 5) can detect minor Fe^{2+} in the crystal structure and be partly attributed to the 0.45 ± 0.02 wt% FeO determined by the electron microprobe measurements. TIR emissivity measurements and diagnostic spectral features are consistent with high-Ca plagioclase (Fig. 5). Across TIR wavelengths, it has been demonstrated that the position of diagnostic spectral features (i.e., Christiansen feature, vibration bands, and transparency feature) shift as a function of An# (Nash and Salisbury 1991; Milam et al. 2004; Donaldson Hanna et al. 2012). Therefore, when comparing laboratory measurements to remote sensing observations, lunar material analogs need to have compositions similar to the Moon, like the Miyake-jima anorthites. Thus, Miyake-jima anorthite megacrysts are unique because they have the necessary spectral features of crystalline, highly calcic anorthite across the NIR and TIR spectral ranges for use as a spectral material analog for the Moon.

Implications

Natural phenocrystic plagioclase crystals typically show some form of growth zoning (e.g., oscillatory zoning) due to the lack of chemical equilibration and sluggish diffusion kinetics. In that light, the homogeneous cores of the Miyake-jima anorthite crystals are unusual since they do not show any evidence of magmatic zoning except for the narrow bytownite rims. These anorthites have a great value and potential to be used as an analog or standard material because they have achieved intragranular and intergranular chemical homogeneity due to their overlapping compositions (Fig. 6) within 1σ uncertainties. The average Miyake-jima anorthite core composition with 1σ uncertainties for the seven individual grains is $An_{95.51\pm0.31}$.

The highly homogeneous characteristics of the Miyake-jima anorthite crystals and their composition resembling lunar anorthites provide a strong rationale for their potential applications in experimental petrology, SIMS analyses, remote sensing, and geophysics. The applications discussed for Miyake-jima anorthite as a lunar material analog can be used to improve the characterization of lunar crustal material, thereby improving our current understanding of the formation and evolution of lunar crust.

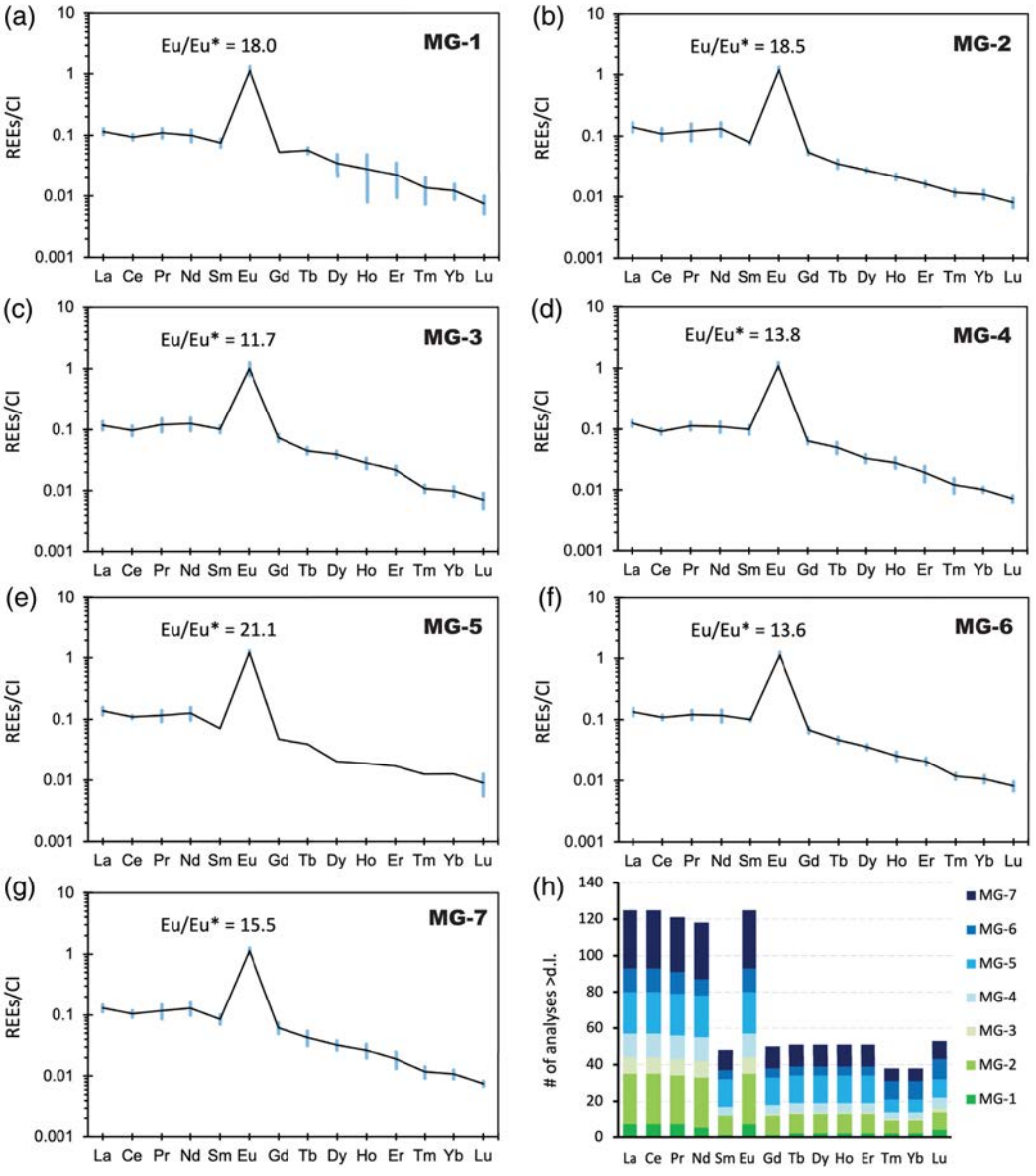

Figure 7. (**a**–**g**) Average chondrite-normalized (McDonough and Sun 1995) REE patterns of the seven individual Miyake-jima crystals with their 1σ standard deviation (blue bars) calculated from each line analyses made for different Miyake-jima grains, and (**h**) the number of analyses (above detection limit) used in the construction of the REE patterns. (Color online.)

Application in experimental petrology

The unaltered and highly homogeneous nature of the major elements (Ca, Si, Al, and Na) of the Miyake-jima crystal cores render them useful as starting materials for experimental studies. Their close match with lunar anorthite compositions in terms of anorthite contents of $An_{96–98}$ (Papike et al. 1997; McGee 1993) also makes them suitable for experimental studies focused on lunar petrology. Although we observe the presence of bytownite rims in the margins of two of the seven selected samples, their volume contribution would have a negligible effect on the bulk anorthite composition of the starting material. Under lunar lower crustal conditions of ~0.3 GPa, the An_{95} solidus temperature is >1500 °C (Lindsley 1969). The large pristine crack-free megacrysts may be used to fabricate capsules in lunar crustal assimilation experiments due to the refractory nature of highly calcic plagioclase. Figure 8 illustrates that Miyake-jima core anorthite contents are similar to the low-anorthite tail of lunar FAN compositions. The cores are slightly enhanced in FeO by ~3.9 times and indistinguishable in MgO content compared to plagioclase from ferroan anorthosites.

The concentrations of REEs in the Miyake-jima crystals are 3–6 times lower than that in FAN, high-magnesium suite (HMS), and high alkali suite (HAS), as illustrated in Figure 9. Most trace elements (see Fig. 10) are within or below the lunar plagioclase concentration range, except for Li and Sr, which approach the upper boundary of the lunar FAN sample suite.

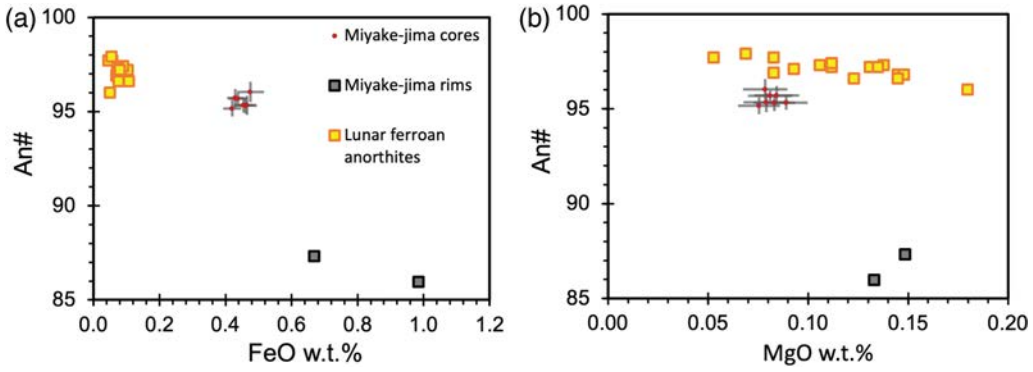

Figure 8. Anorthite content vs. (**a**) FeO and (**b**) MgO wt% (from electron microprobe) for Miyake-jima cores and rims compared to lunar ferroan anorthosites (FAN). Gray error bars show 1σ standard errors on major element and anorthite concentrations. FAN major element composition is based on Papike et al. (1997) and McGee (1993) that include a compilation of analyses performed on lunar FAN plagioclase from samples 60025, 15415, 60015, 60055, 60215, 61016, 62255, 64425, 64435, 65035, 65315, 67525, 67535, 67536, 68515, and 69955. (Color online.)

Also, the trace element concentrations across the grains have a low dispersion (the largest percent standard deviation recorded among the LREEs was ~31%; see Table 5) and show a homogeneous distribution of major, minor, and trace elements in the crystal. The low trace element concentrations compared to lunar plagioclase, the relative homogeneity in trace elements across grains, and their megacrystic occurrence render the Miyake-jima anorthite crystals as an ideal "blank" that can be doped with trace elements as needed for chemical and spectroscopic studies applicable for high-anorthite lunar plagioclase compositions. Day et al. (2019) report 3.64 ppm of copper in the bulk lunar anorthosite measurement from 66095 or "Rusty Rock," which is comparable with the Miyake-jima copper concentrations of 1.40–1.43 ppm (Table 6). Furthermore, considering that Murakami et al. (1991) identified copper inclusions in the Miyake-jima samples, it is probably best not to use Miyake-jima anorthites as a blank slate for copper. A specific REE or any trace element (except copper) with a low abundance may be artificially doped within these plagioclase crystals to elevate their abundances closer to lunar suites (FAN/HMS/HAS), making them more representative. In experiments involving lunar petrology, the trace element concentrations of Miyake-jima anorthites can be adjusted as desired since this study reports what the "blank" levels are, to begin with.

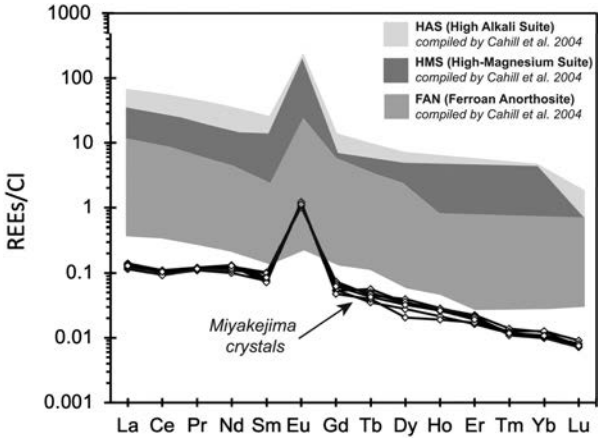

Figure 9. Comparison of CI-normalized REE concentrations of Miyake-jima anorthites and lunar plagioclase grains (compiled by Cahill et al. 2004). REE concentrations of ferroan anorthosite (FAN), high-magnesium suite (HMS), and high-alkali suite (HAS) were compiled from: Floss et al. (1998); Papike et al. (1997, 1996); Shervais and McGee (1998, 1999).

Application as standard reference material for secondary ion mass spectrometry (SIMS)

The most accurate SIMS analyses use matrix-matched (mineralogically and chemically consistent) standards and analytes because secondary ion yields often vary with major element chemistry (e.g., Shimizu and Hart 1982; Mosenfelder et al. 2015). The viability of using Miyake-jima anorthites ("GRR1968" as described in Mosenfelder et al. 2015) for measuring hydrogen in lunar plagioclase has already been demonstrated by Hui et al. (2017). Hydrogen abundances determined by FTIR range from 58 ± 6 to 73 ± 8 ppmw for Miyake-jima anorthites (Mosenfelder et al. 2015). Although the core-rim heterogeneity for H has not yet been investigated for Miyake-jima anorthites, we report in this study that the cores are homogeneous in terms of major and trace elements (see Figs. 2 and 4). This provides a uniform matrix-matched substrate that can be dehydrated to make blanks and doped/implanted with desired trace elements to synthesize appropriate lunar crustal reference materials for future SIMS or nanoSIMS investigations.

Yurimoto et al. (2011) measured the oxygen isotopic composition of Miyake-jima anorthite to be $\delta^{17}O_{SMOW} = 3.33 \pm 0.3‰$ (2σ) and $\delta^{18}O_{SMOW} = 6.40 \pm 0.4‰$ (2σ), which shows a high degree of sample homogeneity and demonstrates its potential use as a standard material for SIMS measurements. Our thorough investigation of the major element chemistry highlights that the homogeneous matrix is well suited for ion microprobe analyses. LaTourrette and Wasserburg (1998) have successfully exploited the homogeneous nature of Miyake-jima anorthite to their advantage and measured diffusion coefficients of Mg, Ca, and Sr using SIMS to understand the thermal evolution of early-formed planetesimals.

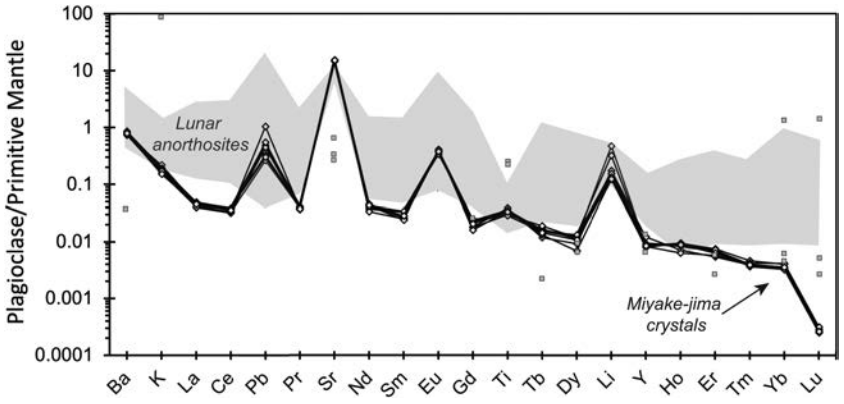

Figure 10. Average primitive mantle-normalized (McDonough and Sun 1995) spidergrams of the seven individual Miyake-jima crystals. Li and K values are from SIMS analyses, while other trace elements are from LA-ICP-MS analyses. The gray field shows trace element concentrations of the lunar anorthosite suites from the literature. Li data for FAN represents solution LA-ICP-MS measurements from 62255 and 65315 reported by Magna et al. (2006). Other FAN trace elements were measured by LA-ICP-MS of plagioclase mineral separates of 15415, Apollo 16 return samples (Pernet-Fisher et al. 2019), and also included the REE compilation by Cahill et al. (2004). Data points identified as outliers with respect to the majority of the samples have been marked as points (gray squares).

Application to remote sensing observations of the Moon and other airless bodies

Across the near-infrared portion of the electromagnetic spectrum, crystalline plagioclase feldspars can be identified by their characteristic 1.25 μm spectral feature owing to minor amounts of Fe^{2+} in the crystal structure. The wavelength position of the 1.25 μm absorption band does not systematically change with calcium content (Adams and Goullaud 1978). Thus, its wavelength position cannot be used to uniquely determine the An# of plagioclase feldspar. Several factors can affect the depth of the 1.25 μm absorption band on the Moon and other airless bodies. First, the depth of the band has been shown to systematically increase with a higher abundance of Fe incorporated into the crystal structure (e.g., Cheek et al. 2010, 2011). Second, the 1.25 μm absorption band can be weakened (i.e., reduced in intensity) to the point of disappearance by space weathering (e.g., Lucey 2002) and shock metamorphism (e.g., Spudis et al. 1984). At thermal infrared wavelengths, the wavelength position of diagnostic spectral features, including the Christiansen feature, fundamental vibration bands (also known as the reststrahlen bands), and the transparency feature, have been shown to shift systematically to higher frequencies (longer wavelengths) as the calcium content in plagioclase feldspar increases (Nash and Salisbury 1991; Milam et al. 2004; Donaldson Hanna et al. 2012). The spectral features, in particular the vibration bands and transparency feature, identified in the Miyake-jima anorthite TIR emissivity spectra are at higher frequencies (longer wavelengths) than previously studied terrestrial anorthite samples that are less calcic than Miyake-jima anorthites. Additionally, the crystalline nature of the Miyake-jima megacrysts results in TIR spectra with more distinct spectral features than previous lab studies of terrestrial anorthites. All of this suggests that lab measurements of Miyake-jima anorthite spectra are necessary for interpreting future hyperspectral observations of the Moon, especially regions identified as pure anorthosites (PANs; e.g., Ohtake et al. 2009; Cheek et al. 2013; Donaldson Hanna et al. 2014).

To best interpret remote sensing observations of the Moon's primary anorthositic crust, especially those that include near- and thermal infrared observations, the plagioclase terrestrial material analog being used must be: (1) crystalline and (2) have an Ohtaki# similar to that of plagioclase within the FANs. Currently, the only known terrestrial material analog that fits these parameters is the Miyake-jima anorthite megacryst (assuming the basaltic coating and mafic inclusions have been removed). Initial laboratory studies have begun with the pure mineral end-member of Miyake anorthite (Donaldson Hanna et al. 2014) and with mixtures of Miyake anorthite and mafic minerals olivine and pyroxene (Arnold et al. 2016; Greenhagen et al. 2020). Future comparisons of NIR and TIR remote sensing observations of the Moon and laboratory measurements of these material analog samples will be critical in better understanding the formation and evolution of the anorthositic crust and the distribution of crustal materials across the lunar surface.

Application to geophysical properties

Branlund and Hofmeister (2012) measured thermal diffusivity (D) of anorthite with Miyake-jima samples between 298–1050 K. They also note low-D_{298} values compared to other plagioclase compositions, along with variation along different crystallographic axes with D_{298} values ranging from 0.682–0.755. Understanding the thermal properties of Miyake-jima anorthite can improve our understanding of conductive heat transfer through the lunar anorthosite "crustal lid" and model the thermal state of the Moon's interior from the time of the magma ocean to the present. Additionally, the Miyake-jima anorthites can also be used to constrain electric resistivities, which in turn have direct application in understanding the nature of the present-day selenotherm (or thermal state) since the bulk of the lunar crust is dominated by anorthositic plagioclase.

Wang et al. (1973) measured the elastic properties of aggregates of plagioclase that have been coupled with seismic discontinuities to understand the crustal structure and density of microcracks in the lunar interior. The study of the elastic properties of Miyake-jima anorthites, which is a closer compositional and structural match with the FAN suites, can potentially improve the current understanding of the seismic signals from the shallow lunar crust. Finally, since the densely cratered structure of the Moon's older FAN highlands would most certainly have evidence of shock features, Miyake-jima crystals can be a great analog for studying the impact history of the lunar crust (Pernet-Fisher et al. 2017). Shocked Miyake-jima samples have been used to derive the Hugoniot equation (Boslough et al. 1986)

and the effect of shock on the Raman spectra (Xie et al. 2021), which highlight Miyake-jima anorthites as a popular choice in understanding shocked feldspars as analogs of the lunar crust.

Acknowledgments and Funding

We thank Eric Fritz from the University of Arizona Alfie Norville Gem and Mineral Museum in Tucson for the gem-quality crystals of Miyake-jima anorthite. The Miyake-jima megacrysts for spectral analyses were obtained from Alfredo Petrov. For support and assistance with analytical techniques, we thank Kenneth Domanik (electron microprobe, University of Arizona) and Lynda Williams (SIMS, Arizona State University, supported by NSF EAR 1819550). We acknowledge Jessica Barnes (University of Arizona) for teaching us how to mount samples in indium. We extend our gratitude to Jan Fietzke (GEOMAR Helmholtz Center for Ocean Research, Kiel) and Jason Kirk (University of Arizona) for constructive feedback on expected challenges in LA-ICPMS for low-signal trace element measurement work undertaken in this study. We also thank Thomas Prettyman (Planetary Science Institute) for providing valuable feedback regarding the application of these samples in spectroscopy. We acknowledge the insightful comments from an anonymous reviewer, Neil Bennett, and Associate Editor Daniel Hummer. A.R. acknowledges support from the Galileo Circle scholarships and the Mineralogical Society of America grant for student research in Mineralogy and Petrology. A.M. acknowledges NASA grant# 80NSSC24K0543 and a startup grant from the Office for Research, Innovation, and Impact and Eminent Scholar Funds from the College of Science at the University of Arizona.

References Cited

Adams, J.B. and Goullaud, L.H. (1978) Plagioclase feldspars—Visible and near infrared diffuse reflectance spectra as applied to remote sensing. *9th Lunar and Planetary Science Conference*, 3, 2901–2909.

Amma-Miyasaka, M. and Nakagawa, M. (2002) Origin of anorthite and olivine megacrysts in island-arc tholeiites: Petrological study of 1940 and 1962 ejecta from Miyake-jima volcano, Izu-Mariana arc. Journal of Volcanology and Geothermal Research, 117, 263–283, https://doi.org/10.1016/S0377-0273(02)00224-X.

Arakawa, Y., Murakami, H., Kimata, M., and Shimoda, S. (1992) Strontium isotope compositions of anorthite and olivine phenocrysts in basaltic lavas and scorias of Miyakejima volcano, Japan. Journal of Mineralogy, Petrology and Economic Geology, 87, 226–239, https://doi.org/10.2465/ganko.87.226.

Arculus, R.J. and Wills, K.J.A. (1980) The petrology of plutonic blocks and inclusions from the Lesser Antilles Island Arc. Journal of Petrology, 21, 743–799, https://doi.org/10.1093/petrology/21.4.743.

Arnold, J.A., Glotch, T.D., Lucey, P.G., Song, E., Thomas, I.R., Bowles, N.E., and Greenhagen, B.T. (2016) Constraints on olivine-rich rock types on the Moon as observed by Diviner and M3: Implications for the formation of the lunar crust. Journal of Geophysical Research: Planets, 121, 1342–1361, https://doi.org/10.1002/2015JE004874.

Bédard, J.H. (2006) Trace element partitioning in plagioclase feldspar. Geochimica et Cosmochimica Acta, 70, 3717–3742, https://doi.org/10.1016/j.gca.2006.05.003.

Behr, W.M., Thomas, J.B., and Hervig, R.L. (2011) Calibrating Ti concentrations in quartz for SIMS determinations using NIST silicate glasses and application to the TitaniQ geothermobarometer. American Mineralogist, 96, 1100–1106, https://doi.org/10.2138/am.2011.3702.

Bindeman, I.N. (2007) Erratum to I.N. Bindeman, A.M. Davis, and M.J. Drake (1998), "Ion microprobe study of plagioclase-basalt partition experiments at natural concentration levels of trace elements," Geochimica Cosmochimica Acta 62, 1175–1193. Geochimica et Cosmochimica Acta, 71, 2414, https://doi.org/10.1016/j.gca.2007.02.003.

Bindeman, I.N. and Davis, A.M. (2000) Trace element partitioning between plagioclase and melt: Investigation of dopant influence on partition behavior. Geochimica et Cosmochimica Acta, 64, 2863–2878, https://doi.org/10.1016/S0016-7037(00)00389-6.

Bindeman, I.N., Davis, A.M., and Drake, M.J. (1998) Ion microprobe study of plagioclase-basalt partition experiments at natural concentration levels of trace elements. Geochimica et Cosmochimica Acta, 62, 1175–1193, https://doi.org/10.1016/S0016-7037(98)00047-7.

Blundy, J.D. and Wood, B.J. (1991) Crystal-chemical controls on the partitioning of Sr and Ba between plagioclase feldspar, silicate melts, and hydrothermal solutions. Geochimica et Cosmochimica Acta, 55, 193–209, https://doi.org/10.1016/0016-7037(91)90411-W.

Boslough, M.B., Rigden, S.M., and Ahrens, T.J. (1986) Hugoniot equation of state of anorthite glass and lunar anorthosite. Geophysical Journal International, 84, 455–473, https://doi.org/10.1111/j.1365-246X.1986.tb04366.x.

Bowen, N.L. (1917) The problem of the anorthosites. The Journal of Geology, 25, 209–243, https://doi.org/10.1086/622473.

Branlund, J.M. and Hofmeister, A.M. (2012) Heat transfer in plagioclase feldspars. American Mineralogist, 97, 1145–1154, https://doi.org/10.2138/am.2012.3986.

Brophy, J.G. (1986) The Cold Bay Volcanic Center, Aleutian Volcanic Arc. Contributions to Mineralogy and Petrology, 93, 368–380, https://doi.org/10.1007/BF00389395.

Brydges, T.F.V., Marriner, C.M., Donaldson Hanna, K.L., Bowles, N.E., and MacDonald R. (2015) Characterisation of Miyake-Jima Anorthite as a lunar analogue. *46th Lunar and Planetary Science Conference*, 1251.

Cahill, J.T., Floss, C., Anand, M., Taylor, L.A., Nazarov, M.A., and Cohen, B.A. (2004) Petrogenesis of lunar highlands meteorites: Dhofar 025, Dhofar 081, Dar al Gani 262, and Dar al Gani 400. Meteoritics & Planetary Science, 39, 503–529, https://doi.org/10.1111/j.1945-5100.2004.tb00916.x.

Cheek, L.C. and Pieters, C.M. (2014) Reflectance spectroscopy of plagioclase-dominated mineral mixtures: Implications for characterizing lunar anorthosites remotely. American Mineralogist, 99, 1871–1892, https://doi.org/10.2138/am-2014-4785.

Cheek, L.C., Parman, S.W., and Pieters, C.M. (2010) Iron in plagioclase: Synthesis experiments with applications to lunar reflectance spectroscopy. In *AGU Fall Meeting Abstracts*, V21E-2370.

Cheek, L.C., Pieters, C.M., Parman, S.W., Dyar, M.D., Speicher, E.A., and Cooper, R.F. (2011) Anorthite synthesis experiments with application to lunar spectroscopy. *41st Lunar and Planetary Science Conference*, 2438.

Cheek, L.C., Donaldson Hanna, K.L., Pieters, C.M., Head, J.W., and Whitten, J.L. (2013) The distribution and purity of anorthosite across the Orientale basin: New perspectives from Moon Mineralogy Mapper data. Journal of Geophysical Research: Planets, 118, 1805–1820, https://doi.org/10.1002/jgre.20126.

Day, J.M.D., Sossi, P.A., Shearer, C.K., and Moynier, F. (2019) Volatile distributions in and on the Moon revealed by Cu and Fe isotopes in the 'Rusty Rock' 66095. Geochimica et Cosmochimica Acta, 266, 131–143, https://doi.org/10.1016/j.gca.2019.02.036.

Dohmen, R. and Blundy, J. (2014) A predictive thermodynamic model for element partitioning between plagioclase and melt as a function of pressure, temperature and composition. American Journal of Science, 314, 1319–1372, https://doi.org/10.2475/09.2014.04.

Donaldson, C.H. and Brown, R.W. (1977) Refractory megacrysts and magnesium-rich melt inclusions within spinel in oceanic tholeiites: Indicators of magma mixing and parental magma composition. Earth and Planetary Science Letters, 37, 81–89, https://doi.org/10.1016/0012-821X(77)90148-0.

Donaldson Hanna, K.L., Wyatt, M.B., Thomas, I.R., Bowles, N.E., Greenhagen, B.T., Maturilli, A., Helbert, J., and Paige, D.A. (2012) Thermal infrared emissivity measurements under a simulated lunar environment: Application to the Diviner Lunar Radiometer Experiment. Journal of Geophysical Research: Solid Earth, 117, E00H05, https://doi.org/10.1029/2011JE003862.

Donaldson Hanna, K.L., Cheek, L.C., Pieters, C.M., Mustard, J.F., Greenhagen, B.T., Thomas, I.R., and Bowles, N.E. (2014) Global assessment of pure crystalline plagioclase across the Moon and implications for the evolution of the primary crust. Journal of Geophysical Research. Planets, 119, 1516–1545, https://doi.org/10.1002/2013JE004476.

Donaldson Hanna, K.L., Greenhagen, B.T., Patterson, W.R. III, Pieters, C.M., Mustard, J.F., Bowles, N.E., Paige, D.A., Glotch, T.D., and Thompson, C. (2017) Effects of varying environmental conditions on emissivity spectra of bulk lunar soils: Application to Diviner thermal infrared observations of the Moon. Icarus, 283, 326–342, https://doi.org/10.1016/j.icarus.2016.05.034.

Donaldson Hanna, K.L., Bowles, N.E., Warren, T.J., Hamilton, V.E., Schrader, D.L., McCoy, T.J., Temple, J., Clack, A., Calcutt, S., and Lauretta, D.S. (2021) Spectral characterization of Bennu analogs using PASCALE: A new experimental set-up for simulating the near-surface conditions of airless bodies. Journal of Geophysical Research: Planets, 126, e2020JE006624.

Dowty, E., Prinz, M., and Keil, K. (1974) Ferroan anorthosite: A widespread and distinctive lunar rock type. Earth and Planetary Science Letters, 24, 15–25, https://doi.org/10.1016/0012-821X(74)90003-X.

Drake, M.J. and Weill, D.F. (1975) Partition of Sr, Ba, Ca, Y, Eu^{2+}, Eu^{3+}, and other REE between plagioclase feldspar and magmatic liquid: An experimental study. Geochimica et Cosmochimica Acta, 39, 689–712, https://doi.org/10.1016/0016-7037(75)90011-3.

Elardo, S.M., Shearer, C.K., and McCubbin, F.M. (2017) The role of KREEP in the production of Mg-suite magmas and its influence on the extent of Mg-suite magmatism in the lunar crust. *48th Lunar And Planetary Science Conference*, JSC-CN-38651.

Elardo, S.M., Laneuville, M., McCubbin, F.M., and Shearer, C.K. (2020) Early crust building enhanced on the Moon's nearside by mantle melting-point depression. Nature Geoscience, 13, 339–343, https://doi.org/10.1038/s41561-020-0559-4.

Falloon, T.J. and Crawford, A.J. (1991) The petrogenesis of high-calcium boninite lavas dredged from the northern Tonga ridge. Earth and Planetary Science Letters, 102, 375–394, https://doi.org/10.1016/0012-821X(91)90030-L.

Fietzke, J. and Frische, M. (2016) Experimental evaluation of elemental behavior during LA-ICP-MS: Influences of plasma conditions and limits of plasma robustness. Journal of Analytical Atomic Spectrometry, 31, 234–244, https://doi.org/10.1039/C5JA00253B.

Floss, C., James, O.B., McGee, J.J., and Crozaz, G. (1998) Lunar ferroan anorthosite petrogenesis: Clues from trace element distributions in FAN subgroups. Geochimica et Cosmochimica Acta, 62, 1255–1283, https://doi.org/10.1016/S0016-7037(98)00031-3.

Foley, S., Tiepolo, M., and Vannucci, R. (2002) Growth of early continental crust controlled by melting of amphibolite in subduction zones. Nature, 417, 837–840, https://doi.org/10.1038/nature00799.

Gao, S., Liu, X., Yuan, H., Hattendorf, B., Günther, D., Chen, L., and Hu, S. (2002) Determination of forty two major and trace elements in USGS and NIST SRM glasses by Laser Ablation-Inductively Coupled Plasma-Mass Spectrometry. Geostandards Newsletter, 26, 181–196, https://doi.org/10.1111/j.1751-908X.2002.tb00886.x.

Greenhagen, B.T., Wagoner, C., Yasanayake, C.N., Donaldson Hanna, K., Bowles, N.E., and Lucey, P.G. (2020) Thermal infrared spectra of lunar analog mineral mixtures under simulated airless body conditions and comparison to LRO Diviner observations. American Geophysical Union, Fall Meeting 2020, P079–0016.

Grove, T.L. and Krawczynski, M.J. (2009) Lunar mare volcanism: Where did the magmas come from? Elements, 5, 29–34, https://doi.org/10.2113/gselements.5.1.29.

Günther, D., Frischknecht, R., Heinrich, C.A., and Kahlert, H.-J. (1997) Capabilities of an argon fluoride 193 nm excimer laser for laser ablation inductively coupled plasma mass spectrometry microanalysis of geological materials. Journal of Analytical Atomic Spectrometry, 12, 939–944, https://doi.org/10.1039/A701423F.

Heinrich, C.A., Pettke, T., Halter, W.E., Aigner-Torres, M., Audétat, A., Günther, D., Hattendorf, B., Bleiner, D., Guillong, M., and Horn, I. (2003) Quantitative multi-element analysis of minerals, fluid and melt inclusions by laser-ablation inductively-coupled-plasma mass-spectrometry. Geochimica et Cosmochimica Acta, 67, 3473–3497, https://doi.org/10.1016/S0016-7037(03)00084-X.

Herzberg, C. and Rudnick, R. (2012) Formation of cratonic lithosphere: An integrated thermal and petrological model. Lithos, 149, 4–15, https://doi.org/10.1016/j.lithos.2012.01.010.

Hui, H., Guan, Y., Chen, Y., Peslier, A.H., Zhang, Y., Liu, Y., Flemming, R.L., Rossman, G.R., Eiler, J.M., Neal, C.R., and others. (2017) A heterogeneous lunar interior for hydrogen isotopes as revealed by the lunar highlands samples. Earth and Planetary Science Letters, 473, 14–23, https://doi.org/10.1016/j.epsl.2017.05.029.

Isshiki, N. (1958) Notes on rock-forming minerals (3) red coloration of anorthite from Hachijojima. Chishitsugaku Zasshi, 64, 644–647.

Kikuchi, Y. (1888) On anorthite from Miyakejima. The Journal of the College of Science, Imperial University of Tokyo, Japan, 2, 31–47.

Kimata, M., Nishida, N., Shimizu, M., Saito, S., Matsui, T., and Arakawa, Y. (1995) Anorthite megacrysts from island arc basalts. Mineralogical Magazine, 59, 1–14, https://doi.org/10.1180/minmag.1995.59.394.01.

LaTourrette, T. and Wasserburg, G.J. (1998) Mg diffusion in anorthite: implications for the formation of early solar system planetesimals. Earth and Planetary Science Letters, 158, 91–108.

Lindsley, D.H. (1969) Melting relations of plagioclase at high pressures, Origin of anorthosite and related rocks. New York State Museum and Science Service, 18, 39–46.

Lucey, P.G. (2002) Radiative transfer model constraints on the shock state of remotely sensed lunar anorthosites. Geophysical Research Letters, 29, 124-1–124-3.

Magna, T., Wiechert, U., and Halliday, A.N. (2006) New constraints on the lithium isotope compositions of the Moon and terrestrial planets. Earth and Planetary Science Letters, 243, 336–353, https://doi.org/10.1016/j.epsl.2006.01.005.

May, T.W. and Wiedmeyer, R.H. (1998) A table of polyatomic interferences in ICP-MS. Atomic Spectroscopy, 19, 150–155.

McDonough, W.F. and Sun, S. (1995) The composition of the Earth. Chemical Geology, 120, 223–253, https://doi.org/10.1016/0009-2541(94)00140-4.

McGee, J.J. (1993) Lunar ferroan anorthosites: Mineralogy, compositional variations, and petrogenesis. Journal of Geophysical Research: Solid Earth, 98, 9089–9105, https://doi.org/10.1029/93JE00400.

Milam, K.A., McSween, H.Y. Jr., Hamilton, V.E., Moersch, J.M., and Christensen, P.R. (2004) Accuracy of plagioclase compositions from laboratory and Mars spacecraft thermal emission spectra. Journal of Geophysical Research: Solid Earth, 109, E04001, https://doi.org/10.1029/2003JE002097.

Mosenfelder, J.L., Rossman, G.R., and Johnson, E.A. (2015) Hydrous species in feldspars: A reassessment based on FTIR and SIMS. American Mineralogist, 100, 1209–1221, https://doi.org/10.2138/am-2015-5034.

Murakami, H., Kimata, M., and Shimoda, S. (1991) Native copper included by anorthite from the island of Miyakejima: Implications for arc magmatism. Journal of Mineralogy, Petrology and Economic Geology, 86, 364–374, https://doi.org/10.2465/ganko.86.364.

Nash, D.B. and Salisbury, J.W. (1991) Infrared reflectance spectra (2.2–15 μm) of plagioclase feldspars. Geophysical Research Letters, 18, 1151–1154, https://doi.org/10.1029/91GL01008.

Ohtake, M., Matsunaga, T., Haruyama, J., Yokota, Y., Morota, T., Honda, C., Ogawa, Y., Torii, M., Miyamoto, H., Arai, T., and others. (2009) The global distribution of pure anorthosite on the Moon. Nature, 461, 236–240, https://doi.org/10.1038/nature08317.

Papike, J.J., Fowler, G.W., Shearer, C.K., and Layne, G.D. (1996) Ion microprobe investigation of plagioclase and orthopyroxene from lunar Mg-suite norites: Implications for calculating parental melt REE concentrations and for assessing postcrystallization REE redistribution. Geochimica et Cosmochimica Acta, 60, 3967–3978, https://doi.org/10.1016/0016-7037(96)00212-8.

Papike, J.J., Fowler, G.W., and Shearer, C.K. (1997) Evolution of the lunar crust: SIMS study of plagioclase from ferroan anorthosites. Geochimica et Cosmochimica Acta, 61, 2343–2350, https://doi.org/10.1016/S0016-7037(97)00086-0.

Paton, C., Hellstrom, J., Paul, B., Woodhead, J., and Hergt, J. (2011) Iolite: Freeware for the visualisation and processing of mass spectrometric data. Journal of Analytical Atomic Spectrometry, 26, 2508–2518, https://doi.org/10.1039/c1ja10172b.

Pernet-Fisher, J.F., Joy, K.H., Martin, D.J.P., and Donaldson Hanna, K.L. (2017) Assessing the shock state of the lunar highlands: Implications for the petrogenesis and chronology of crustal anorthosites. Scientific Reports, 7, 5888, https://doi.org/10.1038/s41598-017-06134-x.

Pernet-Fisher, J.F., Deloule, E., and Joy, K.H. (2019) Evidence of chemical heterogeneity within lunar anorthosite parental magmas. Geochimica et Cosmochimica Acta, 266, 109–130, https://doi.org/10.1016/j.gca.2019.03.033.

Pettke, T., Oberli, F., Audétat, A., Guillong, M., Simon, A.C., Hanley, J.J., and Klemm, L.M. (2012) Recent developments in element concentration and isotope ratio analysis of individual fluid inclusions by laser ablation single and multiple collector ICP-MS. Ore Geology Reviews, 44, 10–38, https://doi.org/10.1016/j.oregeorev.2011.11.001.

Pouchou, J.-L. and Pichoir, F. (1991) Quantitative analysis of homogeneous or stratified microvolumes applying the model "PAP." In K.F.J. Heinrich and D.E. Newbury, Eds., Electron Probe Quantitation, p. 31–75. Springer.

Ramsey, M.S. and Christensen, P.R. (1998) Mineral abundance determination: Quantitative deconvolution of thermal emission spectra. Journal of Geophysical Research: Solid Earth, 103, 577–596, https://doi.org/10.1029/97JB02784.

Ruff, S.W., Christensen, P.R., Barbera, P.W., and Anderson, D.L. (1997) Quantitative thermal emission spectroscopy of minerals: A laboratory technique for measurement and calibration. Journal of Geophysical Research: Solid Earth, 102, 14899–14913, https://doi.org/10.1029/97JB00593.

Salpas, P.A., Haskin, L.A., and McCallum, I.S. (1983) Stillwater Anorthosites: A lunar analog? Journal of Geophysical Research: Solid Earth, 88, B27–B39, https://doi.org/10.1029/JB088iS01p00B27.

Shamloo, H.I., Till, C.B., and Hervig, R.L. (2021) Multi-mode magnesium diffusion in sanidine: Applications for geospeedometry in magmatic systems. Geochimica et Cosmochimica Acta, 298, 55–69, https://doi.org/10.1016/j.gca.2021.01.044.

Shearer, C.K. (2006) Thermal and magmatic evolution of the Moon. Reviews in Mineralogy and Geochemistry, 60, 365–518, https://doi.org/10.2138/rmg.2006.60.4.

Shervais, J.W. and McGee, J.J. (1998) Ion and electron microprobe study of troctolites, norite, and anorthosites from Apollo 14: Evidence for urKREEP assimilation during petrogenesis of Apollo 14 Mg-suite rocks. Geochimica et Cosmochimica Acta, 62, 3009–3023, https://doi.org/10.1016/S0016-7037(98)00195-1.

——— (1999) KREEP cumulates in the western lunar highlands; ion and electron microprobe study of alkali-suite anorthosites and norites from Apollo 12 and 14. American Mineralogist, 84, 806–820, https://doi.org/10.2138/am-1999-5-615.

Shimizu, N. and Hart, S.R. (1982) Applications of the ion microprobe to geochemistry and cosmochemistry. Annual Review of Earth and Planetary Sciences, 10, 483–526, https://doi.org/10.1146/annurev.ea.10.050182.002411.

Sisson, T.W. and Grove, T.L. (1993) Experimental investigations of the role of H_2O in calc-alkaline differentiation and subduction zone magmatism. Contributions to Mineralogy and Petrology, 113, 143–166, https://doi.org/10.1007/BF00283225.

Smith, J.V., Anderson, A.T., Newton, R.C., Olsen, E.J., and Wyllie, P.J. (1970) A petrologic model for the moon based on petrogenesis, experimental petrology, and physical properties. The Journal of Geology, 78, 381–405.

Spudis, P.D., Hawke, B.R., and Lucey, P. (1984) Composition of orientale basin deposits and implications for the lunar basin-forming process. Journal of Geophysical Research: Solid Earth, 89, C197.

Stakes, D.S., Shervais, J.W., and Hopson, C.A. (1984) The volcanic-tectonic cycle of the FAMOUS and AMAR Valleys, Mid-Atlantic Ridge (36°47′N): Evidence from basalt glass and phenocryst compositional variations for a steady state magma chamber beneath the valley midsections, AMAR 3. Journal of Geophysical Research: Solid Earth, 89, 6995–7028, https://doi.org/10.1029/JB089iB08p06995.

Sun, C., Graff, M., and Liang, Y. (2017) Trace element partitioning between plagioclase and silicate melt: The importance of temperature and plagioclase composition, with implications for terrestrial and lunar magmatism. Geochimica et Cosmochimica Acta, 206, 273–295, https://doi.org/10.1016/j.gca.2017.03.003.

Tepley, F.J. III, Lundstrom, C.C., McDonough, W.F., and Thompson, A. (2010) Trace element partitioning between high-An plagioclase and basaltic to basaltic andesite melt at 1 atmosphere pressure. Lithos, 118, 82–94, https://doi.org/10.1016/j.lithos.2010.04.001.

Thomas, I.R., Greenhagen, B.T., Bowles, N.E., Donaldson Hanna, K.L., Temple, J., and Calcutt, S.B. (2012) A new experimental setup for making thermal emission measurements in a simulated lunar environment. The Review of Scientific Instruments, 83, 124502, https://doi.org/10.1063/1.4769084.

Walker, D. and Hays, J.F. (1977) Plagioclase flotation and lunar crust formation. Geology, 5, 425–428, https://doi.org/10.1130/0091-7613(1977)5%3C425:PFALCF%3E2.0.CO;2.

Walker, F., Lee, M., and Parsons, I. (1995) Micropores and micropermeable texture in alkali feldspars: Geochemical and geophysical implications. Mineralogical Magazine, 59, 505–534, https://doi.org/10.1180/minmag.1995.059.396.12.

Wang, H., Todd, T., Richter, D., and Simmons, G. (1973) Elastic properties of plagioclase aggregates and seismic velocities in the moon. *Proceedings of the Lunar Science Conference*, 4, 2663.

Warren, P.H. (1985) The magma ocean concept and lunar evolution. Annual Review of Earth and Planetary Sciences, 13, 201–240, https://doi.org/10.1146/annurev.ea.13.050185.001221.

Williams, J.P., Paige, D.A., Greenhagen, B.T., and Sefton-Nash, E. (2017) The global surface temperatures of the Moon as measured by the Diviner Lunar Radiometer Experiment. Icarus, 283, 300–325, https://doi.org/10.1016/j.icarus.2016.08.012.

Wood, J.A., Dickey, J.S. Jr., Marvin, U.B., and Powell, B.N. (1970) Lunar anorthosites and a geophysical model of the Moon. *Proceedings of the Apollo 11 Lunar Science Conference*, 1, 965–988.

Woodhead, J.D., Hellstrom, J., Hergt, J.M., Greig, A., and Maas, R. (2007) Isotopic and elemental imaging of geological materials by laser ablation inductively coupled plasma-mass spectrometry. Geostandards and Geoanalytical Research, 31, 331–343, https://doi.org/10.1111/j.1751-908X.2007.00104.x.

Xie, T., Osinski, G.R., and Shieh, S.R. (2021) Raman study of shock effects in lunar anorthite from the Apollo missions. Meteoritics & Planetary Science, 56, 1633–1651, https://doi.org/10.1111/maps.13728.

Yurimoto, H., Abe, K., Abe, M., Ebihara, M., Fujimura, A., Hashiguchi, M., Hashizume, K., Ireland, T.R., Itoh, S., Katayama, J., and others. (2011) Oxygen isotopic compositions of asteroidal materials returned from Itokawa by the Hayabusa mission. Science, 333, 1116–1119, https://doi.org/10.1126/science.1207776.

Manuscript received July 12, 2023
Manuscript accepted May 7, 2024
Accepted manuscript online May 14, 2024
Manuscript Handled by Daniel hummer

Endnotes:

[1]Deposit item AM-25-19122. Dataset available: Miyake-jima Anorthite: A Lunar Crustal Material Analog, University of Arizona Research Data Repository, https://doi.org/10.25422/azu.data.23671140.v1. Online Materials are free to all readers. Go online, via the table of contents or article view, and find the tab or link for supplemental materials.